6-1-2013

Marine Low Cloud Sensitivity to An Idealized Climate Change: The CGILS LES Intercomparison

Peter N. Blossey
University of Washington, pblossey@uw.edu

Christopher S. Bretherton
University of Washington

Minghua Zhang
Stony Brook University

Anning Cheng
Science Systems and Applications, Inc.,

Satoshi Endo
Brookhaven National Laboratory

Publisher's Statement

Open Access

Marine low cloud sensitivity to an idealized climate change: The CGILS LES intercomparison

Peter N. Blossey,[1] Christopher S. Bretherton,[1] Minghua Zhang,[2] Anning Cheng,[3] Satoshi Endo,[4] Thijs Heus,[5] Yangang Liu,[4] Adrian P. Lock,[6] Stephan R. de Roode,[7] and Kuan-Man Xu[8]

Received 31 July 2012; revised 4 February 2013; accepted 20 February 2013; published 14 May 2013.

[1] Subtropical marine low cloud sensitivity to an idealized climate change is compared in six large-eddy simulation (LES) models as part of CGILS. July cloud cover is simulated at three locations over the subtropical northeast Pacific Ocean, which are typified by cold sea surface temperatures (SSTs) under well-mixed stratocumulus, cool SSTs under decoupled stratocumulus, and shallow cumulus clouds overlying warmer SSTs. The idealized climate change includes a uniform 2 K SST increase with corresponding moist-adiabatic warming aloft and subsidence changes, but no change in free-tropospheric relative humidity, surface wind speed, or CO_2. For each case, realistic advective forcings and boundary conditions are generated for the control and perturbed states which each LES runs for 10 days into a quasi-steady state. For the control climate, the LESs correctly produce the expected cloud type at all three locations. With the perturbed forcings, all models simulate boundary-layer deepening due to reduced subsidence in the warmer climate, with less deepening at the warm-SST location due to regulation by precipitation. The models do not show a consistent response of liquid water path and albedo in the perturbed climate, though the majority predict cloud thickening (negative cloud feedback) at the cold-SST location and slight cloud thinning (positive cloud feedback) at the cool-SST and warm-SST locations. In perturbed climate simulations at the cold-SST location without the subsidence decrease, cloud albedo consistently decreases across the models. Thus, boundary-layer cloud feedback on climate change involves compensating thermodynamic and dynamic effects of warming and may interact with patterns of subsidence change.

Citation: Blossey, P. N., C. S. Bretherton, M. Zhang, A. Cheng, S. Endo, T. Heus, Y. Liu, A. P. Lock, S. R. de Roode, and K.-M. Xu (2013), Marine low cloud sensitivity to an idealized climate change: The CGILS LES intercomparison, *J. Adv. Model. Earth Syst.*, *5*, 234–258, doi:10.1002/jame.20025.

1. Introduction

[2] Uncertainties in cloud feedbacks in global climate models remain a major uncertainty, despite much progress in the representation of clouds over the past decades [*Soden and Held*, 2006]. Low clouds in particular are responsible for much of the variability in cloud feedbacks among the coupled ocean-atmosphere climate models that participated in the last two rounds of the coupled model intercomparison project, CMIP3 [*Soden and Vecchi*, 2011] and CMIP5 [*Andrews et al.*, 2012]. *Bony and Dufresne* [2005] found much of this variability arose from intermodel differences in the climate change response of marine boundary-layer cloud in low-latitude ocean regions under mean subsidence.

[3] Because the turbulence that sustains this cloud is not resolved by the grid of atmospheric general circulation models (GCMs), it is simulated using interacting parameterizations for boundary-layer turbulence, cumulus convection, cloud microphysics, and subgrid distribution of cloud, each of which can be quite intricate. *Zhang and Bretherton* [2008] showed how the complex interplay between these parameterizations can affect simulated cloud feedbacks in an idealized single-column climate change scenario. Although contemporary GCMs simulate the present-day geographical and

[1]Department of Atmospheric Sciences, University of Washington, Seattle, Washington, USA.
[2]School of Marine and Atmospheric Sciences, Stony Brook University, Stony Brook New York, USA.
[3]Science Systems and Applications, Inc., Hampton, Virginia, USA.
[4]Atmospheric Sciences Division, Brookhaven National Laboratory, Upton New York, USA.
[5]Max-Planck-Institut für Meteorologie, Hamburg, Germany.
[6]Foundation Science, Met Office, Exeter, UK.
[7]Department of Multi-Scale Physics, Delft University of Technology, Delft, Netherlands.
[8]Science Directorate, NASA Langley Research Center, Hampton, Virginia, USA.

1942-2466/13/jame.20025

seasonal distribution of low cloud with increasing realism [*Klein et al*., 2012], the range of GCM-simulated cloud feedbacks remains as wide as ever. Cleverly chosen observational proxies may prove a useful model constraint to help narrow this range, but so far they have proved elusive due to an inadequate understanding of the underlying low cloud feedback mechanisms.

[4] One strategy that is becoming more popular is to use large-eddy simulation (LES) of boundary-layer cloudiness. LES is an attractive tool because it can explicitly simulate the cloud-turbulence interaction that is the key to the structure of subtropical cloud-topped boundary layers, and has been shown to realistically simulate key boundary-layer cloud types and their transitions [e.g., *Caldwell and Bretherton*, 2009; *Berner et al*., 2011; *Sandu and Stevens*, 2011]. Several recent studies have compared LES results somehow representing a control and perturbed climate [e.g., *Blossey et al*., 2009; *Xu et al*., 2010; *Rieck et al*., 2012]. These studies have reached a variety of conclusions about the sign and amplitude of the simulated low cloud feedbacks which are difficult to synthesize because they used different control states, different forcing perturbations, and different models.

[5] This provides fertile ground for an intercomparison of the sensitivity of boundary-layer clouds simulated by different LES models to some standardized idealized climate changes. Such a study aims to test whether different LES models produce the same low cloud feedback to a given climate perturbation, and if so, what feedback mechanisms are at work.

1.1. CGILS and Its LES Component

[6] This paper reports on the results of the LES component of the CFMIP/GASS Intercomparison of Large-Eddy and Single-Column Models (CGILS), a collaboration between two organizations, the Cloud Feedbacks Model Intercomparison Project (CFMIP) and the Global Atmospheric Systems Studies (GASS), within the World Climate Research Program. The goal of CGILS is to identify the physical processes responsible for cloud feedbacks over the subtropical oceans and to evaluate the representation of those processes in single-column models (SCMs) and their parent global climate models. The strategy is to use SCMs and LESs to simulate the cloud response to tightly controlled idealized climate perturbations representative of the effects of greenhouse warming by comparing simulations with large-scale forcings and boundary conditions from a control climate to simulations with perturbed forcings and boundary conditions from a warmed climate. The tacit hypothesis is that the response of the boundary-layer clouds to the change in these forcings is the critical uncertainty in representing their feedbacks with climate change. The design of the CGILS intercomparison is described in detail by M. Zhang et al. (CGILS: First results from an international project to understand the physical mechanisms of low cloud feedbacks in general circulation models, submitted to *Bulletin of the American Meteorological Society*, 2012, herein referred to as Zhang et al., submitted manuscript, 2012) and will only be summarized here.

[7] In this framework, LESs, which can realistically represent the interactions between boundary-layer clouds and turbulent circulations, are intended to serve as a benchmark for the SCMs, for which such interactions are not resolved and must be treated through assumptions built into the SCM moist physics parameterizations. However, LES are not substitutes for reality. Each LES still has a suite of microphysical, subgrid turbulence, surface flux and radiation parameterizations and schemes for advecting scalars and velocity that can have significant discretization errors in regions with sharp property gradients such as the capping inversion atop a typical marine stratocumulus cloud layer. Past GASS LES intercomparisons have shown that for stratocumulus under a strong inversion, the cloud thickness is sensitive to grid resolution, advection, and subgrid turbulence schemes [e.g., *Bretherton et al*., 1999; *Stevens et al*., 1995; *Cheng et al*., 2010], and for all precipitating boundary-layer cloud types, the cloud properties are sensitive to microphysical parameterizations [e.g., *Ackerman et al*., 2009; *vanZanten et al*., 2011]. Thus another important goal within CGILS is to assess whether the clouds simulated by different LESs all respond in a similar way to a given climate perturbation, and if so, what this might reveal about key mechanisms of subtropical low cloud feedback on climate change.

[8] In CGILS, three cases were generated corresponding to three positions along the GEWEX cloud system study (GCSS) Pacific Cross-Section [*Teixeira et al*., 2011] that extends from off the coast of San Francisco, past Hawaii to the Intertropical Convergence Zone, using July-mean conditions. They are designated S12 (35°N, 125°W), S11 (32°N, 129°W), and S6 (17°N, 149°W). The July climatological cloud regime ranges from shallow stratocumulus at S12 near the California coast to deeper, often decoupled, stratocumulus at S11, which is near the climatological maximum of cloud fraction along the cross section, to shallow cumulus convection at S6 [*Lin et al*., 2009; *Teixeira et al*., 2011]. For LES, as for the first round of SCM intercomparison, only steady, monthly-mean forcings with diurnally averaged insolation were considered to allow robust calculation of small differences in cloud properties between control and perturbed runs using runs of affordable length.

1.2. Organization of This Paper

[9] The present paper intercompares the simulated cloud response at the three locations to a given climate perturbation, using an international group of LES models. It is a companion to Zhang et al. (submitted manuscript, 2012), which gives an overview of the CGILS effort along with initial results and a focus on the intercomparison of SCMs. A second companion paper [*Zhang et al*., 2012] describes the design of the CGILS forcings and the formulation of the idealized climate perturbation. Last, *Bretherton et al*. [2013] considers the low cloud responses of a single-LES model to a variety

of climate perturbations, including several beyond those considered in this intercomparison, and seeks to explain the physical mechanism for the simulated low cloud responses.

[10] In the remainder of this paper, the setup of the CGILS cases are described briefly in section 2, including some additional specifications used for LESs but not for SCMs. The results for the three locations are presented in sections 3–5. Discussion and conclusions are presented in section 6. Details about the case setup and the participating LESs are given in Appendices A and B.

2. Setup of CGILS LES Intercomparison

2.1. Design of Overall CGILS Intercomparison

[11] The specifications of the CGILS SCM intercomparison are discussed by *Zhang et al*. [2012], which provides motivation for details of the choices of control and perturbed forcing profiles. The forcings and specifications for CGILS can also be found at http://atmgcm.msrc.sunysb.edu/cfmip_figs/Case_specification.html. Except as noted in the next section, the LESs were steadily forced similarly to the SCMs.

[12] The abbreviation CTL will be used for control climate simulations, and P2S for the idealized warm-climate simulations. Here "P2" refers to the 2 K sea surface temperature (SST) increase, and "S" refers to the subsidence decrease. A few salient points about the initial conditions and large-scale forcings for these simulations follow.

2.1.1. Control Climate

[13] Reference temperature and humidity profiles for the control climate simulations were derived from ECMWF Interim Reanalysis (ERA) [*Dee et al*., 2011] monthly means for July 2003 at the three locations. At S6, this reference profile was used to initialize the model simulations. At S11 and S12, the model simulations were initialized from initial profiles that included a stratocumulus-capped mixed layer and were derived from the reference profiles for those locations. This initialization enabled comparisons of the initial evolution of the cloud layer in the different models.

[14] The large-scale forcings represent idealizations of those at these locations. The mean subsidence profiles have a fixed vertical structure whose amplitude at each location is adjusted to match results from a blend of ERA and selected climate models, with climate models included here because they inform the change in subsidence in the perturbed climate simulations. At pressures above 900 hPa, the large-scale horizontal temperature and moisture advection profiles are proportional to the SST gradient along the GCSS Pacific Cross-Section *Zhang et al* [2012]. Aloft (at pressures below 800 hPa), the large-scale horizontal advective tendencies are specified to balance the vertical advective tendencies and the clear-sky radiative heating (both estimated from the reference temperature and humidity profiles), so that the free-tropospheric energy and moisture budgets will be in approximate balance. Between 800 and 900 hPa, the large-scale horizontal advective tendencies are interpolated based on pressure.

[15] All large-scale forcings (i.e., large-scale subsidence and large-scale horizontal advection of temperature and moisture) are steady, and diurnally averaged insolation is used.

2.1.2. Perturbed Climate: Warming With Subsidence Change (P2S)

[16] For the perturbed climate, SST is increased by 2 K. The reference temperature profile for P2S is derived by applying a warming perturbation to the CTL reference temperature profile. The temperature is increased uniformly by 2 K up to the lifting condensation level (LCL) and above the LCL, and is increased following a moist pseudoadiabat based on a 2 K surface temperature increase. The reference humidity profile for P2S is specified so that the relative humidity (RH) is identical to that of the CTL reference profiles at all heights. In addition, subsidence is uniformly reduced at all heights by approximately 11% from the control climate, reflecting a blend of climate model results over this region. The reduction in subsidence reflects the expected weakening of the Hadley-Walker circulation in the tropics [e.g., *Vecchi and Soden*, 2007]. This fractional reduction is particularly large over the NE Pacific; it is about twice as large as found in multimodel-mean composites based on the average of comparable low-latitude ocean climate regimes worldwide [*Webb et al*., 2012].

[17] The large-scale horizontal advection of temperature within the boundary layer (proportional to the SST gradient along the GCSS Pacific Cross-Section) is unchanged, as this climate perturbation is modeled after a uniform increase of SST across the tropics. However, the large-scale advection of moisture within the boundary layer increases in magnitude due to Clausius-Clapeyron as it is proportional to the gradient of saturation mixing ratio at the surface. The large-scale horizontal advection of temperature and moisture aloft (i.e., above 800 hPa) is adjusted to balance the free-tropospheric budgets of moisture and energy based on the changed subsidence profiles and P2S reference profiles of temperature and moisture.

2.1.3. Perturbed Climate: Warming Only (P2)

[18] For the coastal stratocumulus case (S12), the LES simulated an additional climate perturbation that includes only the warming perturbation with no change in subsidence. As the appropriate change in subsidence in a warmed climate averaged across the subtropical marine stratocumulus regimes is uncertain and climate model-dependent, this experiment can help separate the sensitivity to warming from that to subsidence changes. As the subsidence warming and drying will differ from the P2S case, the large-scale horizontal advection aloft was changed from the P2S case so that the free troposphere will remain in approximate balance.

[19] Last, note that the perturbed climate simulations in CGILS include several effects (e.g., warming and subsidence) that may be expected to affect low clouds in a perturbed climate but neglect others, such as CO_2 impacts on radiative cooling, changes in estimated inversion strength (EIS) [*Wood and Bretherton*, 2006], changes in surface wind speed, and changes in free-tropospheric RH. A companion study [*Bretherton et al*.,

Table 1. LES Domain Size and Resolution for CGILS Cases

Case	Δx (m)	Δz_{inv} (m)	$L_{x,y}$ (m)	z_{relax}[a] (m)	z^{+}_{relax}[a] (m)	c_T (m s^{-1})	z_1 (m)	D_{srf}[b] (s^{-1})
S6	100	40	9600	4000	4800	0.0081	20	5.25×10^{-6}
S11	50	5[c]	4800	2500	3000	0.0081	12.5	3.25×10^{-6}
S12	25	5[c]	2400	1200	1500	0.0104	2.5	1.68×10^{-6}

[a]Nudging rate increases with height as specified in section A1 from zero at the base of the thermodynamic nudging layer, z_{relax}, to 1 h^{-1} at z^{+}_{relax} and above.
[b]Divergence of the large-scale velocity field at the surface.
[c]LaRC used coarser Δz_{inv} of 25 m in S11 and 7.5 m in S12.

2013] evaluates the individual and combined impact of these climate perturbations using a single-LES model. The effects of transient variability are considered in a second phase of CGILS *Zhang et al*. [2012], but the protocol has not yet been adapted to LES, for which the specified 100 day simulations are computationally challenging, if not intractable.

2.2. Additional LES Case Specifications

[20] The CGILS project took 4 years to reach its present form. Much of the time and effort went into recognizing and removing differences in simulations that were due to inconsistencies between the setups used for particular models that arose mainly from ambiguities in the overall CGILS case specifications. This led to the introduction of several rounds of additional specifications for the LES intercomparison to ensure that the free-tropospheric structure remained realistic and that results would reflect meaningful differences among the LESs in only the advection, subgrid turbulence, and microphysical parameterizations. These additional LES-only specifications included:

[21] 1. LESs were run for 10 days, rather than the SCM specification of 100 days, for computational economy. In most cases, this was long enough for the simulated cloud statistics to reach an approximate quasi-steady state over a long enough period to allow robust differencing between the control and perturbed simulations.

[22] 2. Uniform LES grid resolution and domain size (Table 1).

[23] 3. Lower minimum heights for nudging of free-tropospheric temperature and humidity profiles (Table 1 and section A1).

[24] 4. Common specification for cloud droplet effective radius and partial adoption of a single radiative transfer scheme (section A2).

[25] 5. Uniform bulk surface flux scheme and wind nudging (section A3; bulk transfer coefficients c_T and recommended lowest-grid-level heights z_1 at which they should be applied are given in Table 1).

[26] 6. Climate-dependent minimum free-tropospheric humidity (S12 only; section A4).

[27] 7. Reduced subsidence (S12 only; section A5). The surface horizontal wind divergence implied by the subsidence profile at each location is given in Table 1.

[28] 8. For S11 and S12, the LES were initialized with stratocumulus-capped mixed-layer profiles rather than the reference (ERA) temperature and humidity profiles as in the SCMs. This does not affect the ultimate steady state reached.

[29] 9. The LES performed additional simulations of the warming-only climate perturbation (P2) at S12.

[30] These additional specifications were not used by the CGILS SCM simulations (Zhang et al., in preparation, 2012) but should be used by future SCMs seeking to compare in detail with the CGILS LES results. During this process, several other possible future improvements to the CGILS case specifications were recognized; these are discussed in the conclusions.

2.3. Participating LES Models

[31] An international group of six LES models participated in the CGILS LES intercomparison. Table 2 lists the models, investigators, and their institutional affiliations, as well as the abbreviations used for each LES in this paper. Two models submitted results using both their default advection schemes and an alternative advection schemes. In a variant of SAM, termed SAMA, an alternative scalar advection scheme was used that was designed to be more accurate, including in regions of sharp humidity and temperature gradients such as inversions capping stratocumulus layers or the edges of cumulus clouds. A variant of MOLEM, termed MOLEMA, used a monotonic scheme for both scalar and momentum advections, rather than just for scalar advection. This prevents spurious oscillations in the momentum field near sharp gradients, such as near inversions. Such oscillations in the momentum field can impact the subgrid diffusivity in such regions. These can be used to assess the sensitivity of CGILS results to the choice of LES advection scheme. Appendix B briefly documents each LES.

3. S12: Coastal Stratocumulus

[32] The CGILS forcings and reference profiles for the S12 location, together with the LES initial profiles, are shown in Figure 1.

[33] Recall from section 2.1 that the control (CTL) reference thermodynamic profiles (Figures 1a and 1b) are based on ERA July 2003 mean for this location. They show a time average across shallow boundary layers with a relatively narrow range of inversion heights in the 925 to 975 hPa layer (approximately 400–800 m), as marked by strong vertical gradients of RH and potential temperature θ. As discussed in section 2.2, the simulations at S12 (and also S11) are initialized

Table 2. Abbreviations for CGILS LES Models

Abbreviation	Name	Participants	Institution	Country
DALES	Dutch Atmospheric LES	de Roode	TU Delft	Netherlands
LaRC	Langley Research Center/UCLA LES	Cheng/Xu	NASA LaRC	USA
MOLEM	Met Office Large Eddy Model	Lock	UK Met Office	UK
MOLEMA	MOLEM with ULTIMATE advection for momentum			
SAM	System for Atmospheric Modeling	Blossey	University of Washington	USA
SAMA	SAM with Blossey-Durran advection			
UCLA	Max Planck/UCLA LES	Heus	MPI-Hamburg	Germany
WRF[a]	Weather Research and Forecast Model	Endo/Liu	Brookhaven	USA

[a]S6 only.

using the plotted mixed-layer profiles of θ and RH with an initial inversion height in the middle of the vertical gradient region of the reference profiles. We have tested that the steady states reached by the models do not depend on this choice of initial condition, but it does allow quicker development of a realistic cloud-topped boundary-layer structure than does the CGILS specification of initializing with the ERA reference profiles.

[34] As the large-scale forcings (subsidence and horizontal advection of temperature and moisture) are steady, there is no distinction between their initial and reference values. The mean vertical pressure velocity ω (Figure 1c) increases nearly linearly with height across the boundary layer and peaks at 750 hPa, well above the boundary-layer top. As shown in Figures 1d and 1e, between the surface and 900 hPa, there is uniform cold and dry advection that is (by assumption) slaved to surface SST advection; this transitions to moist advection and even stronger cold advection at pressures below 800 hPa, where the forcings have been constructed to steadily maintain the reference profile. The wind profiles used for wind relaxation are not shown, but the near-surface wind speed is 8.3 m s^{-1}.

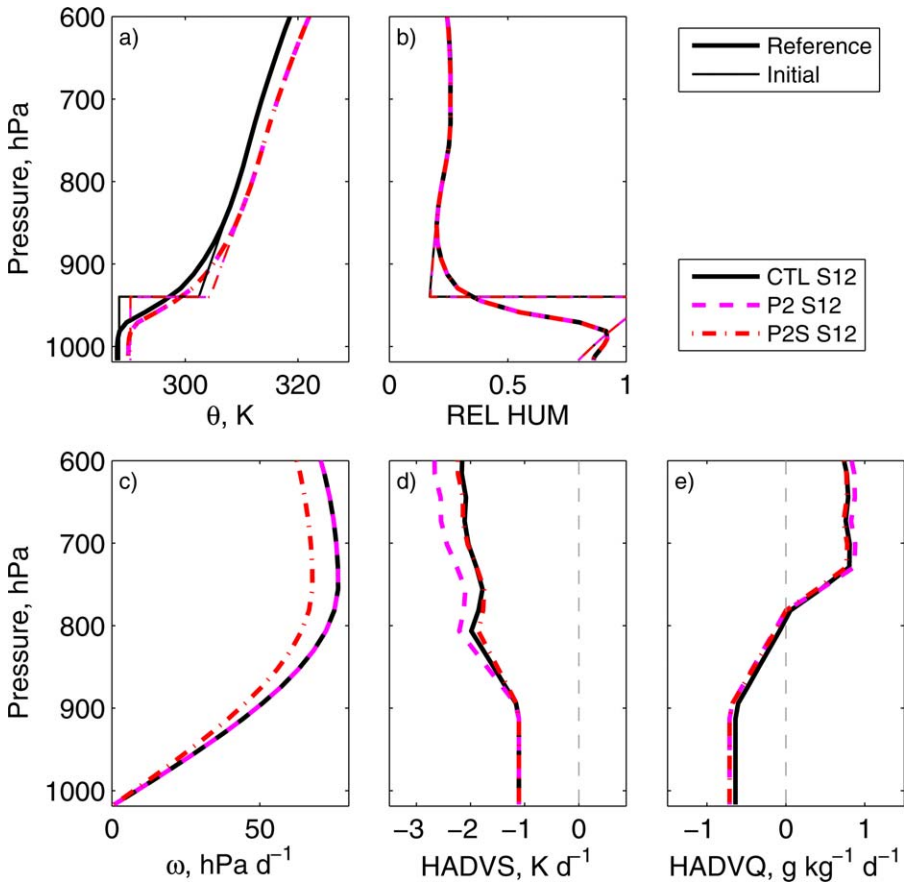

Figure 1. Reference and initial profiles of (a) θ (θ_l for initial profile), (b) RH, (c) mean vertical pressure velocity, and horizontal advection of (d) temperature and (e) humidity, for the CGILS S12 control, warmed-unchanged subsidence (P2), and warmed-climate (P2S) simulations.

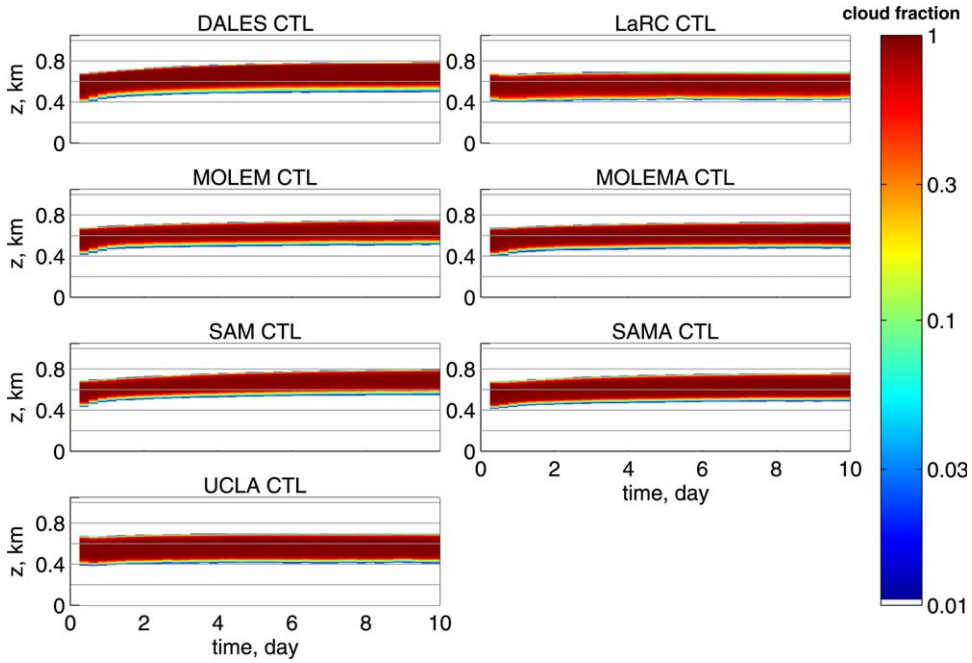

Figure 2. Time-height profiles of cloud fraction for the S12 control simulations. Profiles have been averaged in the x and y directions and in 6 h chunks, as have all quantities in the figures unless otherwise mentioned.

[35] The warmed-climate reference profiles show features of the CGILS idealized climate changes. The θ perturbation is moist-adiabatic, and the RH and wind profiles are unchanged. While the subsidence in the CTL and P2 simulations is identical, the subsidence is uniformly decreased by approximately 11% in the P2S simulations. The low-level horizontal advection of temperature is unchanged from the control due to the CGILS assumption of uniform surface warming throughout the tropics, but the dry advection in the boundary layer is stronger in the warmed climate due to the 7% K^{-1} Clausius-Clapeyron-induced increase of horizontal humidity gradient over warmer SST.

3.1. S12 Control Simulation

[36] Figure 2 shows time-height profiles of cloud fraction from the control simulations of each LES model. Each control simulation lasts 10 days, with each model nearly reaching an equilibrium by the end of the simulation. The time series of cloud liquid water path (LWP) in Figure 3a show that the LWP in the models appears to be in an approximately statistically steady state. The shortwave cloud radiative effect (SWCRE) is stronger (more negative) for models simulating more LWP. This is expected under the full cloud cover simulated by all models for the present case but is a useful test that the shortwave radiation parameterizations and effective

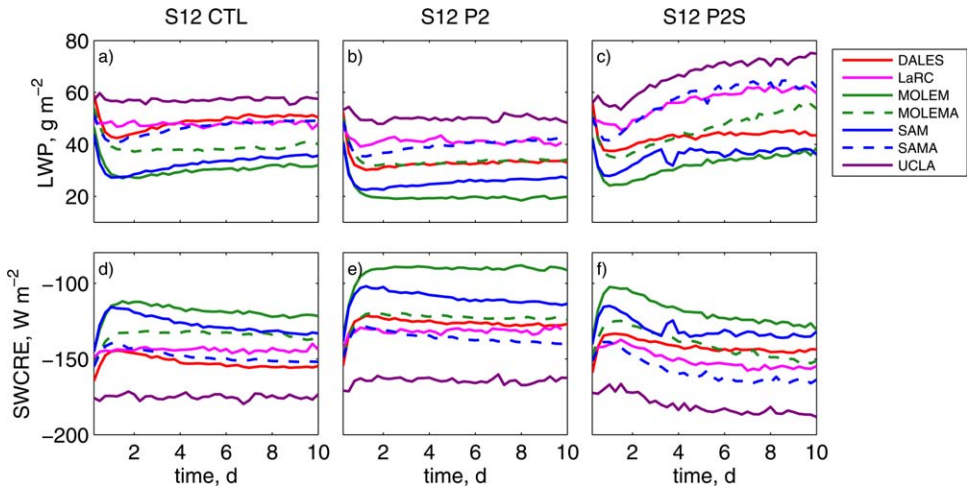

Figure 3. Time series of (a-c) cloud LWP and (d-f) SWCRE for the S12 (a,d) control, (b,e) P2, and (c,f) P2S sensitivity simulations in the CGILS LES intercomparison.

Table 3. Summary of Steady-State (8 to 10 Day Mean) Results for S12

Model	Run Name	z_i (m)	z_b (m)	LCL[a] (m)	w_e (m s^{-1})	SHF (W m^{-2})	LHF (W m^{-2})	QRAD (W m^{-2})	CF (%)	LWP (g m^{-2})	SWCRE (W m^{-2})
DALES	CTL	781	558	552	4.2	1.2	86	−43	100	51	−155
	P2	745	564	564	4.0	1.8	97	−41	100	33	−127
	P2S	878	671	630	4.2	−1.4	101	−39	100	45	−145
LaRC	CTL	690	462	446	3.7	7.9	75	−41	98	48	−144
	P2	683	472	457	3.7	6.8	84	−38	96	41	−131
	P2S	804	558	521	3.8	4.4	88	−38	99	61	−156
MOLEM	CTL	746	557	531	4.0	3.1	83	−40	99	32	−122
	P2	683	528	500	3.7	2.9	87	−34	94	20	−90
	P2S	870	670	607	4.2	−0.2	95	−37	99	37	−127
MOLEMA	CTL	726	521	501	3.9	5.3	82	−41	99	40	−135
	P2	722	536	514	3.9	4.1	91	−39	99	34	−123
	P2S	889	656	609	4.2	0.3	96	−38	100	54	−151
SAM	CTL	790	594	576	4.3	1.0	85	−42	99	36	−133
	P2	752	579	562	4.1	1.5	94	−39	97	27	−113
	P2S	899	701	616	4.3	−0.7	95	−39	100	38	−135
SAMA	CTL	755	526	516	4.1	3.7	83	−43	100	49	−152
	P2	742	531	522	4.0	3.6	93	−41	99	42	−139
	P2S	894	640	608	4.3	−0.3	97	−39	100	63	−164
UCLA	CTL	694	451	437	3.7	5.0	82	−42	100	57	−175
	P2	695	469	454	3.8	4.1	93	−40	99	50	−164
	P2S	814	546	519	3.9	0.5	96	−38	100	73	−186

[a]Computed from mean thermodynamic properties between 100 and 200 m altitude. *Definition of terms:* z_i, inversion height; z_b, stratocumulus cloud base height; LCL, lifting condensation level; w_e, entrainment rate; SHF, sensible heat flux; LHF, latent heat flux; QRAD, radiative flux divergence between surface and inversion; CF, cloud fraction; LWP, liquid water path; SWCRE, shortwave cloud radiative effect.

radius formulations are adequately consistent between the models. The UCLA model appears to have slightly stronger SWCRE for a given LWP than the other models due to unique features of its radiation scheme, which lead to increases in downwelling SW radiative fluxes at the inversion 15–20 W m^{-2} larger than the other models.

[37] Table 3 contains several "steady-state" cloud- and boundary-layer properties averaged over the last 2 days of the control and perturbed simulations; here we consider the control run. The steady-state inversion heights z_i, diagnosed as the level at which mean RH crosses 50%, range between 690 and 788 m, and the LWPs vary from 35 to 57 g m^{-2}; none of the models generate significant precipitation at the surface or at cloud base. This level of consistency between models is excellent by the standard of previous GASS LES intercomparisons of stratocumulus-capped boundary layers [*Stevens et al.*, 1995; *Ackerman et al.*, 2009]. The difference δz_{dcpl} between stratocumulus cloud base height z_b, diagnosed as the highest level below the cloud fraction maximum at which cloud fraction reaches 50% of its maximum value, and the near-surface LCL is a convenient measure of decoupling. For the control run, δz_{dcpl} varies from 0 to 30 m between models. This, along with the final profiles of total water mass mixing ratio and liquid water static energy shown in Figure 4, indicates that the control boundary layer is fairly well mixed in each LES.

[38] Compared to the observed summertime climatology at location S12 [*Lin et al.*, 2009; *Teixeira et al.*, 2011; *Xu and Cheng*, 2013], the steady states of the control simulations have slightly deeper inversion heights, higher cloud fractions, and stronger SWCREs despite smaller LWPs. The stronger SWCRE is due in part to diurnally averaged insolation, which suppresses the observed daytime minimum in stratocumulus LWP, and to the use of the daytime-averaged zenith angle rather than the insolation-weighted zenith angle, which artificially increases the cloud albedo. (See *Bretherton et al.* [2013] for the comparison of runs with and without a diurnal cycle and a discussion of the effect of zenith angle.) We do not expect quantitative agreement between the S12 control simulations and climatology at this location because the simulations do not include transient forcing variability or diurnally varying insolation, and because of the difficulty of representing the sharp inversion atop stratocumulus clouds. We regard the qualitative agreement with observations to be an adequate basis for regarding our sensitivity experiments as meaningful indicators of cloud response in the coastal well-mixed stratocumulus regime.

3.2. Separation of the Thermodynamic Component of Cloud Feedback in S12

[39] The default CGILS climate change consists of a thermodynamic warming and a subsidence reduction, resulting in the perturbed case P2S. For case S12, all LES models also ran case P2, which included the thermodynamic warming but not the subsidence reduction; this is roughly analogous to the partitioning of tropics-wide cloud feedbacks into thermodynamic and dynamic components proposed by *Bony et al.* [2004]. Cloud changes from the CTL to P2 simulations represent a sensitivity to thermodynamic changes, while cloud changes between the P2 and P2S simulations reflect a sensitivity to dynamic (subsidence) changes. The steady-state inversion heights of the cloud-topped boundary layers depicted in Figure 2 reflect an

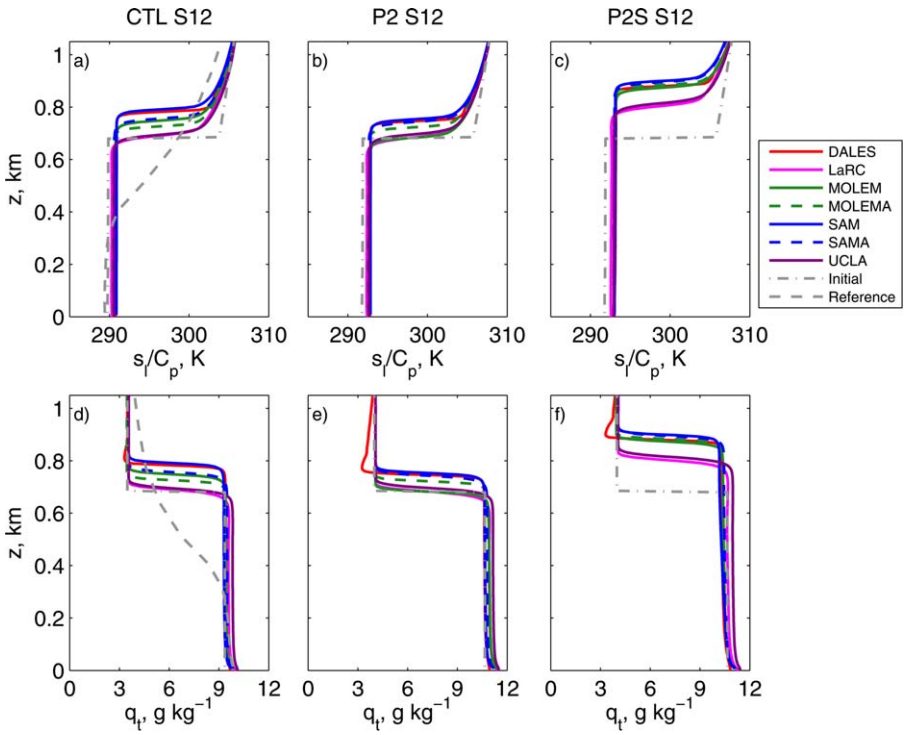

Figure 4. Profiles of (a-c) liquid water static energy divided by c_p and (d-f) total water at the end of the simulations for the S12 (a,d) control, (b,e) P2, and (c,f) P2S sensitivity studies.

equilibrium between entrainment and subsidence at the boundary-layer top, rather than that at the 500 hPa level often used in studies of large-scale circulation changes [e.g., *Vecchi and Soden*, 2007].

[40] Figure 5 depicts profiles of vertical pressure velocity ω as composited over cool regions of the low-latitude oceans from three GCM simulations of a control climate and one with SSTs uniformly raised by 2 K.

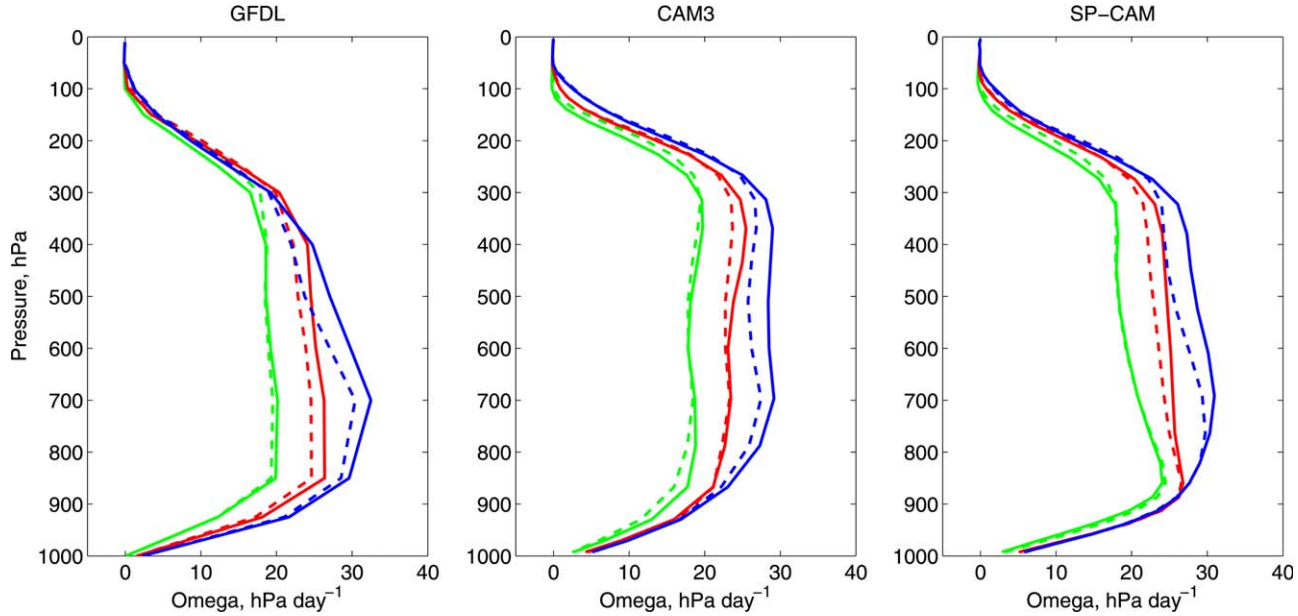

Figure 5. Profiles of monthly-mean ω composited over cool regions of the low-latitude oceans from three global climate models, for control SSTs (solid) and for SST uniformly raised by 2 K (dashed). The regions used for the blue, red, and green curves form the three highest deciles of monthly-mean LTS over ocean locations in 30∘S–30∘N, corresponding to coastal stratocumulus, cumulus-under-stratocumulus, and cumulus cloud regimes, respectively.

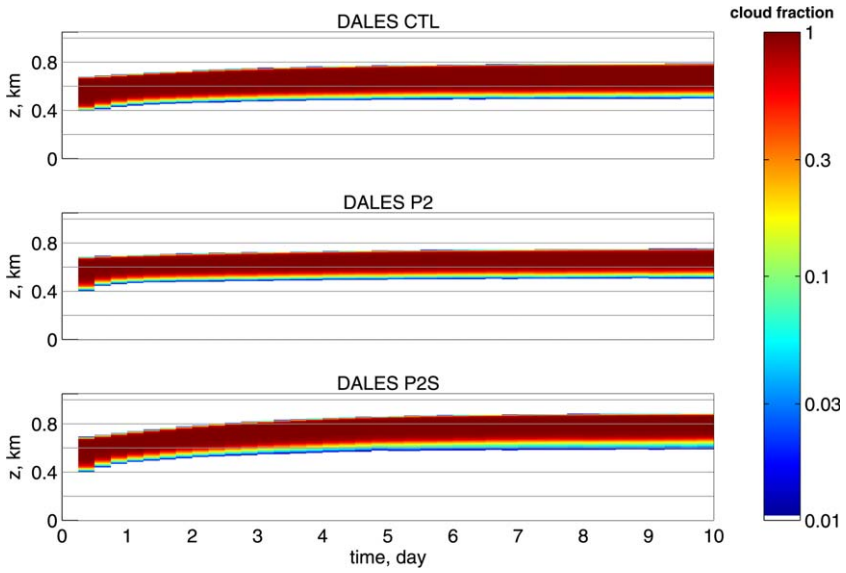

Figure 6. Time-height profiles of cloud fraction for the S12 control, P2, and P2S simulations from DALES.

The selected regions form the three highest deciles of monthly-mean lower-tropospheric stability (LTS) [*Klein and Hartmann*, 1993] over ocean locations in 30°S–30°N, which roughly correspond to the three CGILS cloud regimes [*Blossey et al.*, 2009]. The blue lines indicate the highest decile, which includes the S12 location. For all plotted GCMs, the mid-tropospheric subsidence for this decile is reduced in the warmer climate, as is lower-tropospheric subsidence in the Geophysical Fluid Dynamics Laboratory (GFDL) Atmospheric Model 2.12b and Community Atmosphere Model, version 3, (CAM3) models, but the superparameterized version of the Community Atmosphere Model (SP-CAM) simulates almost no relative reduction of subsidence at typical inversion heights between 800 hPa and the surface, suggesting the plausibility of a scenario like in P2. Separating the sensitivity of low clouds to thermodynamic and dynamic changes may help illuminate the extent to which cloud responses to a climate change are driven by model-to-model differences in large-scale forcing [*Caldwell et al.*, 2012] versus differences in the boundary-layer response to a given forcing (the CGILS approach). The present approach is extended by *Bretherton et al.* [2013], who consider the sensitivity of the CGILS cases to a number of other climate perturbations, both thermodynamic (e.g., radiative effects of CO_2) and dynamic (e.g., changes in wind speed).

3.3. Cases P2 and P2S: Warming Without and With Subsidence Changes

[41] Figure 6 shows time-height cross sections of cloud fraction from the CTL, P2, and P2S simulations from DALES; these are broadly representative of the evolution of all the models. The inversion rises slightly to comparable steady-state heights in CTL and P2, but the cloud layer becomes slightly thinner in P2. In contrast, the cloud layer thickens in the P2S simulation, as the marine boundary layer deepens more strongly than in the other cases. The sharp transition in cloud fraction across the mean cloud base in CTL and P2 is indicative of a well-mixed boundary layer in which all updrafts have a similar LCL; in P2S this transition is less sharp, suggesting incipient decoupling. The P2 and P2S LWP and SWCRE time series in Figure 3b reach near-equilibrium by the end of the run.

3.3.1. LWP Reduction in P2

[42] Table 3 compares the 8 to 10 day means of key variables between P2, P2S, and CTL for each LES. With unchanged subsidence (P2), all models show a significant reduction in LWP (around 10 g m^{-2}) from the control and a corresponding decrease in cloud thickness. The cloud thickness reductions of 7%–20% overwhelm the slight increases in LWP of an adiabatic cloud of fixed thickness in the warmer climate due to changes in the liquid water lapse rate [e.g., *Somerville and Remer*, 1984], changing the sign of the implied cloud feedback from negative to positive. In some but not all of the models, there is also a slight reduction in inversion height and entrainment rate. There is little difference between P2 and CTL in the decoupling measure δz_{dcpl}, suggesting that the reduction in cloud thickness is not related to decoupling.

[43] DALES has an 18 g m^{-2} LWP reduction from CTL to P2, rather larger than the other models. We speculate this may result from its advection scheme. DALES is the only LES among these that does not employ flux correction to suppress spurious extrema due to advection, and q_t undershoots above the inversion are visible in its mean profiles (Figure 4). These undershoots are more severe in the P2 and P2S cases than in the control, artificially drying the entrained air, which would excessively thin the cloud layer [*Bretherton et al.*, 2013].

[44] *Bretherton et al.* [2013] argues based on the SAMA LES results and a mixed-layer model that the decreases in LWP in P2 are due to the reduced radiative

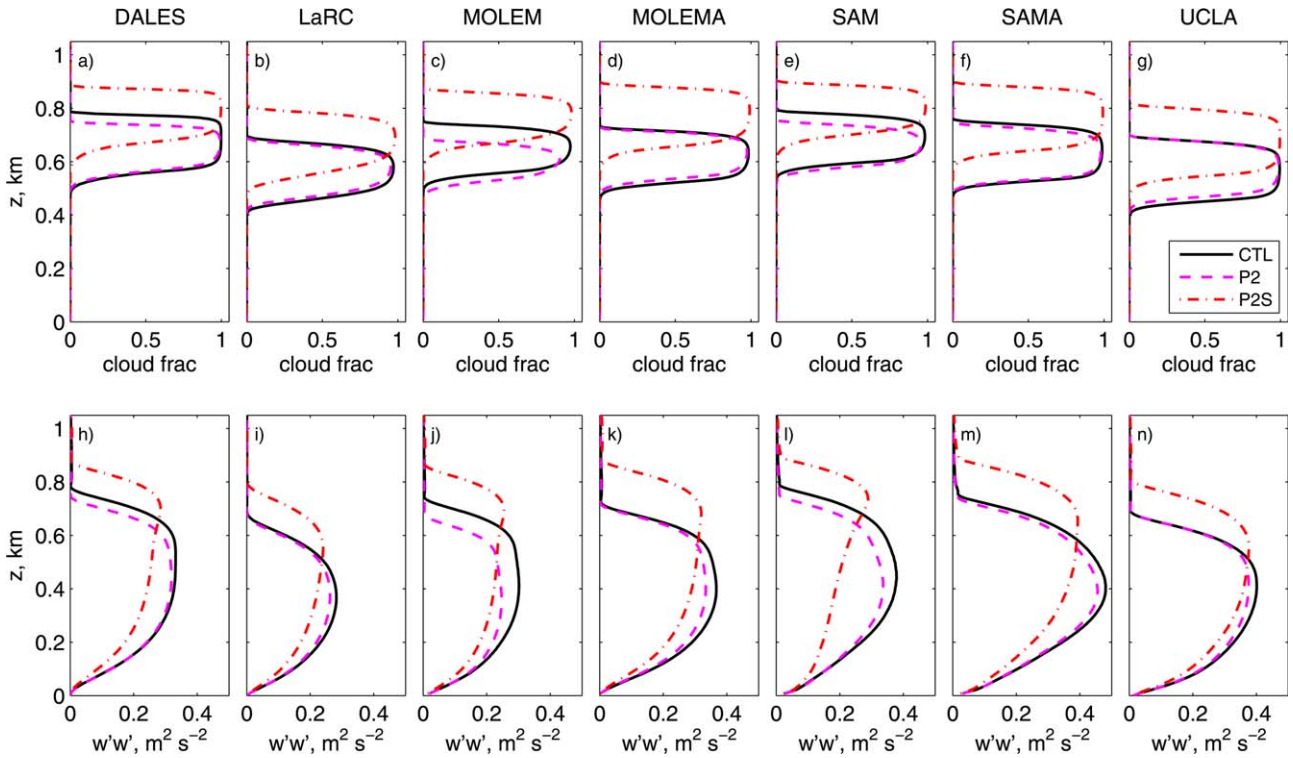

Figure 7. Time-averaged profiles of (a-g) cloud fraction and (h-n) vertical velocity variance for the S12 control, P2, and P2S sensitivity studies from the CGILS LES intercomparison are shown from (a,h) DALES, (b,i) LaRC, (c,j) MOLEM, (d,k) MOLEMA, (e,l) SAM, (f,m) SAMA, and (g,n) UCLA.

cooling of the boundary layer due to the increased longwave opacity of the warmer, moister free troposphere, and the increased humidity difference between the surface and the lower free troposphere. Table 3 lends robustness to the first of these mechanisms because it shows that the boundary-layer-integrated radiative flux divergence QRAD is smaller in P2 than in CTL for all the LES models. The difference is approximately 5% in all models except MOLEM. MOLEM experiences a larger radiative cooling reduction because its cloud fraction decreases from 99% in CTL to 94% in P2, and its LWP also reduces substantially, allowing some reduction in the downwelling longwave radiation at the sea surface due to the holes and thin spots in the cloud. MOLEMA, which maintains a slightly thicker and more solid cloud for all cases due to its use of a monotonic advection scheme for both scalars and momentum, is consistent with the other LES models.

3.3.2. Sensitivity to Subsidence Changes

[45] When the subsidence is reduced in the P2S simulations, the equilibrium cloud top and cloud base heights rise by more than 100 m from their values in the P2 simulations. In all models, the separation δz_{dcpl} between stratocumulus cloud base and the LCL increases (Table 3), suggesting that the deeper boundary layers in the P2S simulations are marginally decoupled, as also suggested by the top-heaviness of the vertical velocity variance profiles in Figure 7.

[46] LWP increases from P2 to P2S by 30%–50%, and SWCRE strengthens by 18–37 W m^{-2}, qualitatively consistent with observational findings of T. A. Myers and J. R. Norris (Observational evidence that enhanced subsidence reduces subtropical marine boundary layer cloudiness, *J. Climate*, in revision, 2013). The contrasting responses of the cloud to thermodynamic and dynamic changes are depicted in Figure 8, where the changes in SWCRE from CTL to P2 and from P2 to P2S are shown as a function of inversion height for each model. While the CTL simulations differ in their equilibrium LWP and inversion height, their responses to thermodynamic and dynamic changes are qualitatively similar.

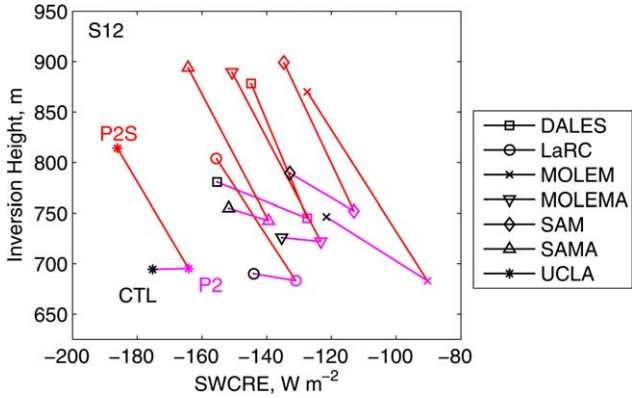

Figure 8. Scatterplot of inversion height (z_i) and SWCRE from the CTL, P2, and P2S simulations for each of the CGILS models at S12. Lines connect the CTL, P2, and P2S simulations from each model.

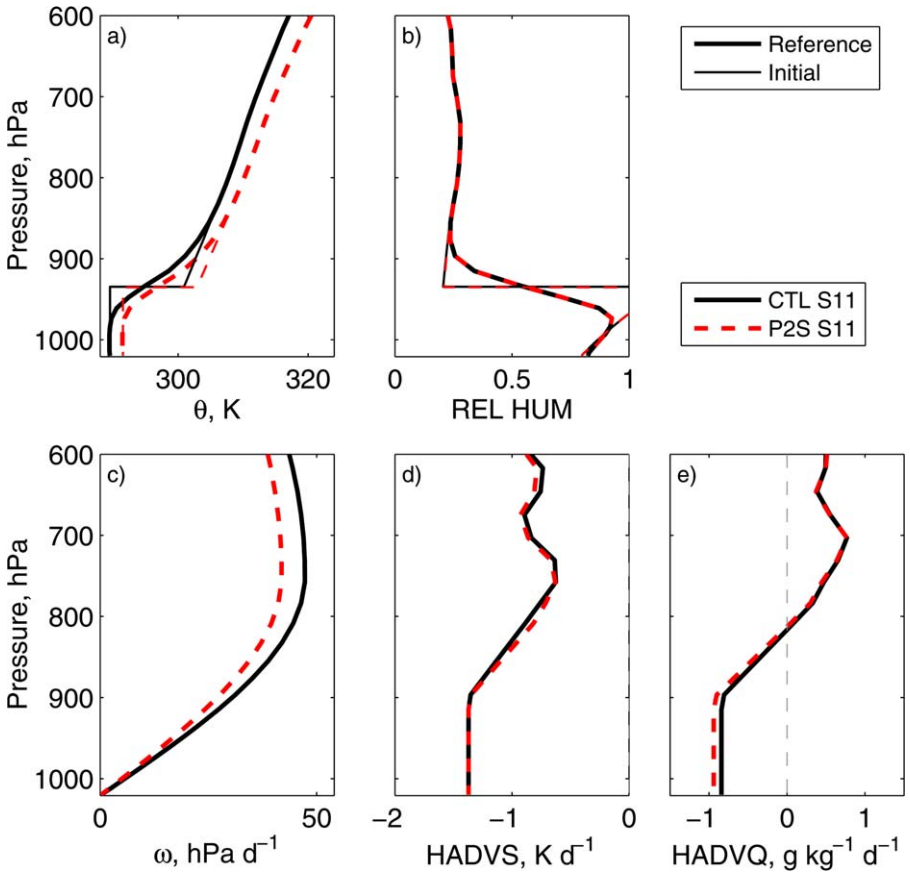

Figure 9. As in Figure 1, but for CGILS S11 control (CTL) and warmed-climate (P2S) simulations.

3.4. Sensitivity to Combined Warming and Subsidence Changes

[47] Compensation between the cloud thinning due to thermodynamic changes (from CTL to P2) and cloud thickening due to subsidence changes (from P2 to P2S) leads to cloud thickness changes of model-dependent sign when the two effects are considered together. All models except DALES have increased LWP and stronger SWCRE in P2S than CTL (subsidence changes dominate thermodynamic changes, creating negative cloud feedback), while in DALES, the thermodynamic changes are stronger. Across the seven models, the SWCRE change from CTL to P2S ranges from −16 to 10 W m^{-2}; an approximate estimate of interquartile range obtained by removing the two extreme models is −12 to −2 W m^{-2}.

[48] *Bretherton et al.* [2013] note that CMIP3 multimodel-mean changes over the subsiding regions of subtropical oceans for CO_2 doubling have somewhat larger thermodynamic changes (approximately 2.5 K) and a subsidence reduction about half as large as that of P2S (approximately 5%). Neglecting the effects of other changes (e.g., CO_2 and EIS) and assuming that the effects of temperature and subsidence changes may be scaled and superposed, this would lead to rather small SWCRE changes from CTL in all models except DALES and MOLEM, for which these changes would be positive. *Bretherton et al.* [2013] argues based on SAMA simulations that the radiative effect of doubled CO_2 would further thin the stratocumulus layer, leading to a significant positive feedback that overwhelms other neglected forcing changes; this would be useful to test in other LES models.

4. S11: Decoupled Stratocumulus

[49] The reference (ERA) and initial profiles and the horizontal advective forcings for the S11 location are shown in Figure 9. The ERA θ and RH profiles imply typical boundary-layer depths in the range 900–950 hPa (approximately 600–1050 m), slightly deeper than at S12. The subsidence is decreased relative to that at S12 by approximately a third, and the LTS is decreased from 25.4 K at S12 to 22.4 K at S11. As at S12, each LES is initialized with a well-mixed boundary layer. For this case and S6, the LES followed the CGILS case outline and only performed CTL and P2S simulations, which combine the cloud responses to thermodynamic and subsidence changes.

4.1. S11 Control Simulation

[50] Time-height profiles of cloud fraction from the control simulations with each LES are displayed in Figure 10. Each model is initialized with full cloud cover, and the inversion height increases over the course of the

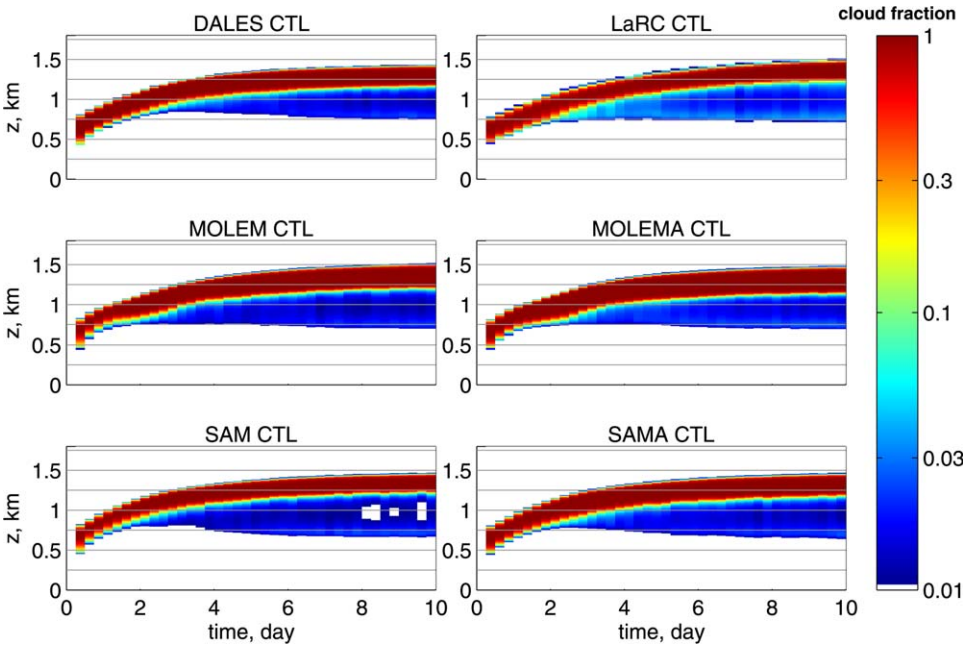

Figure 10. Time-height profiles of cloud fraction for the S11 control simulations in the CGILS LES intercomparison.

runs, reaching 1400–1500 m by the end of the 10 day long simulations. Because of the wide range of inversion heights during the simulations, and because accurate simulation of entrainment rate requires use of a vertically uniform grid throughout the region swept out by the inversion, the S11 simulation was particularly computationally intensive. One of the models, LaRC, used a 25 m vertical grid spacing instead of the 5 m vertical grid spacing employed by the other LES. It remains unclear why the LaRC model, unlike other LES, does not overentrain at 25 m grid spacing [*Bretherton et al.*, 1999]. Results from the UCLA model are not included because its free-tropospheric humidity spuriously drifts away from the reference profile later in the simulation.

[51] As with S12, salient boundary-layer properties averaged over the last 2 days of the 10 day simulations are shown in Table 4. In all of the models, the boundary layer becomes decoupled with a layer of cumulus clouds (low cloud fraction) beneath a stratocumulus layer with full cloud cover. The stratocumulus cloud base height exceeds the LCL by roughly 400–500 m. The profiles of q_t and s_l/c_p in Figure 11 show two well-mixed layers in most of the models, one extending up to the LCL that is driven by surface buoyancy fluxes, overlaid by a second driven by cloud top radiative cooling [*Turton and Nicholls*, 1987]. Figure 12 and Table 4 show that three of the models shown (SAM, DALES, and LaRC) have similar LWP and SWCRE, while SAMA, MOLEM, and MOLEMA support somewhat thicker, brighter stratocumulus layers.

[52] The ERA reference profiles are fairly consistent with various satellite estimates of mean summertime

Table 4. Summary of Steady-State (8 to 10 Day Mean) Results for S11[a]

Model	Simulation Name	z_i (m)	z_b (m)	LCL (m)	w_e (mm s^{-1})	SHF (W m^{-2})	LHF (W m^{-2})	QRAD (W m^{-2})	LWP (g m^{-2})	SWCRE (W m^{-2})
DALES	CTL	1421	1171	785	4.6	4.1	103	−31	52	−156
	P2S	1537	1299	767	4.4	4.2	112	−28	46	−146
LaRC	CTL	1502	1228	720	4.9	5.1	97	−33	51	−152
	P2S	1622	1351	703	4.7	4.8	106	−30	51	−151
MOLEM	CTL	1506	1213	703	4.8	4.2	97	−30	75	−174
	P2S	1644	1359	679	4.7	4.2	105	−27	71	−170
MOLEMA	CTL	1471	1149	710	4.7	4.8	96	−30	93	−188
	P2S	1623	1317	684	4.6	4.7	104	−27	85	−180
SAM	CTL	1455	1232	696	4.7	3.8	97	−32	44	−145
	P2S	1585	1362	675	4.6	3.7	105	−30	45	−146
SAMA	CTL	1453	1186	700	4.7	3.8	97	−33	63	−167
	P2S	1590	1330	674	4.6	3.7	105	−30	62	−165

[a]In all models, the cloud fraction is 100%, and surface precipitation is negligible. *Definition of terms:* z_i, inversion height; z_b, stratocumulus cloud base height; LCL, lifting condensation level; w_e, entrainment rate; SHF, sensible heat flux; LHF, latent heat flux; QRAD, radiative flux divergence between surface and inversion; LWP, liquid water path; SWCRE, shortwave cloud radiative effect.

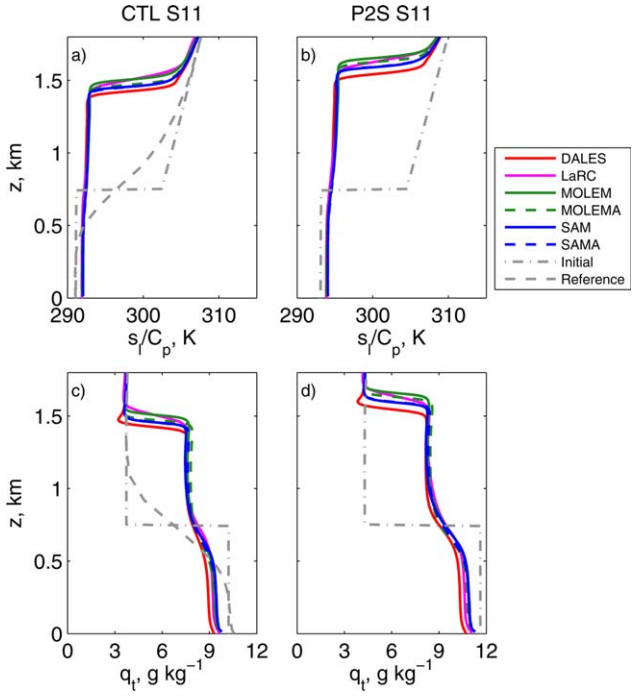

Figure 11. Profiles of (a,b) liquid water static energy divided by c_p and (c,d) total water at the end of the simulations of the S11 (a,c) control and (b,d) P2S sensitivity studies.

boundary-layer height from *Lin et al.* [2009], which ranges from about 700 to 1100 m. The substantial increase in boundary-layer depth in the S11 control simulations away from the ERA climatological reference profiles suggests there may be biases in the CGILS-specified forcings, such as an excessively deep layer of dry and cold advection or inadequate mean horizontal divergence below the trade inversion. Despite the depth of the boundary layer, the full cloud cover and decoupled state of the boundary layer are characteristic of cloud-topped boundary layers across much of the eastern subtropical oceans, so that the study of its sensitivity to an idealized climate perturbation is regarded as meaningful.

[53] As in S12, the near-100% cloud cover simulated by all the models exceeds the summertime average of approximately 85% [*Teixeira et al.*, 2011], the mean LWP is smaller than observed, and the SWCRE is stronger than observed. The possible reasons for the opposite sign of the biases between SWCRE and LWP given in section 3.1 apply equally well to S11 as S12.

4.2. Sensitivity to Combined Warming and Subsidence Changes

[54] Time-height profiles of cloud fraction from CTL and P2S simulations with a representative LES, DALES, are shown in Figure 13. The P2S simulation develops a similar decoupled vertical structure to the control, but due to the subsidence reduction, the inversion height reaches a steady state 120 m above that of the CTL simulation; the other models behave very similarly. The decoupling increases in P2S for all models; the stratocumulus cloud base rises, while the LCL and cumulus cloud base remain nearly unchanged (Figures 14a–14f and Table 4). The enhanced decoupling in P2S is also manifest in the increased q_t and s_l/c_p differences between the surface and cloud layers (Figure 11) and a more pronounced minimum in vertical velocity variance at 700 m in the transition between the two mixed layers (Figures 14g–14l).

[55] Figure 12 shows that the evolution of LWP and SWCRE is similar in the P2S runs to the control runs of SAM, SAMA, and DALES, with an initial transient followed by small variations in LWP as the marine boundary layer deepens. In the P2S simulations of LaRC, MOLEM, and MOLEMA, the LWP increases steadily after initial transients and minima early in the runs. The "steady-state" day 8–10 average LWP changes from CTL to P2S (Table 4) are small in SAM, LaRC, and SAMA, but MOLEM, MOLEMA, and

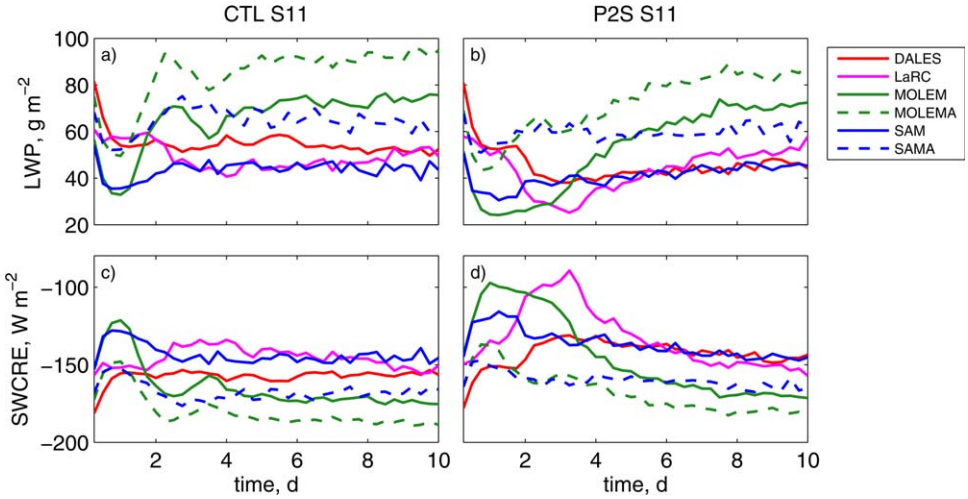

Figure 12. Time series of (a,b) cloud LWP and (c,d) SWCRE for the S11 (a,c) control and (b,d) P2S sensitivity simulations in the CGILS LES intercomparison.

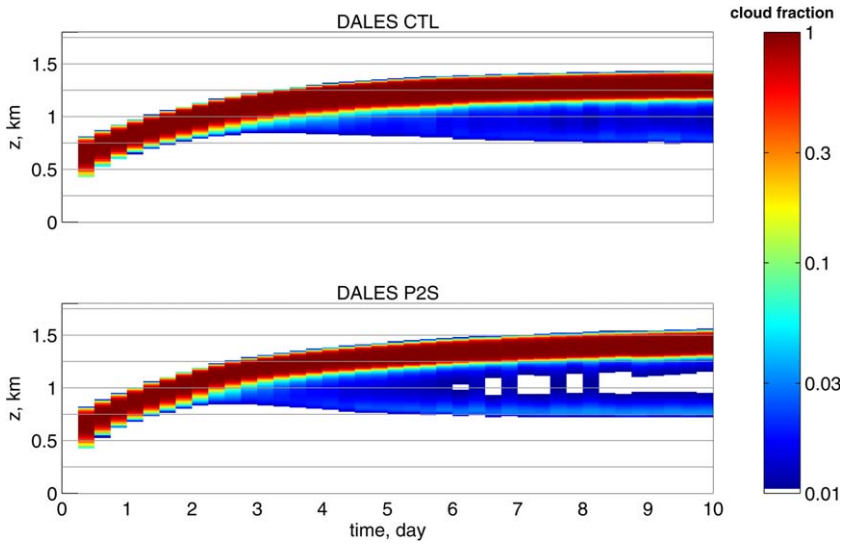

Figure 13. Time-height profiles of cloud fraction for the S11 control and P2S simulations from DALES.

DALES show decreases in LWP that range from 6% to 12%. The strongest decrease in LWP occurs in DALES and is reminiscent of S12; unlike S12, however, the q_t undershoot above the inversion is similar in P2S as in CTL, so changes in the DALES inversion humidity jump from CTL to P2S are similar to the other models. While MOLEM and MOLEMA are among the models with the strongest increases from CTL to P2S in moisture decoupling (measured as the difference in q_t between the subcloud and cloud layers, not shown), SAMA has a similar increase of moisture decoupling and a much smaller LWP change from CTL to P2S than MOLEM and MOLEMA, so that the change in moisture decoupling does not seem to be decisive in the cloud thinning. Overall, it is difficult to pinpoint the mechanisms of cloud thinning in this case. Unlike in

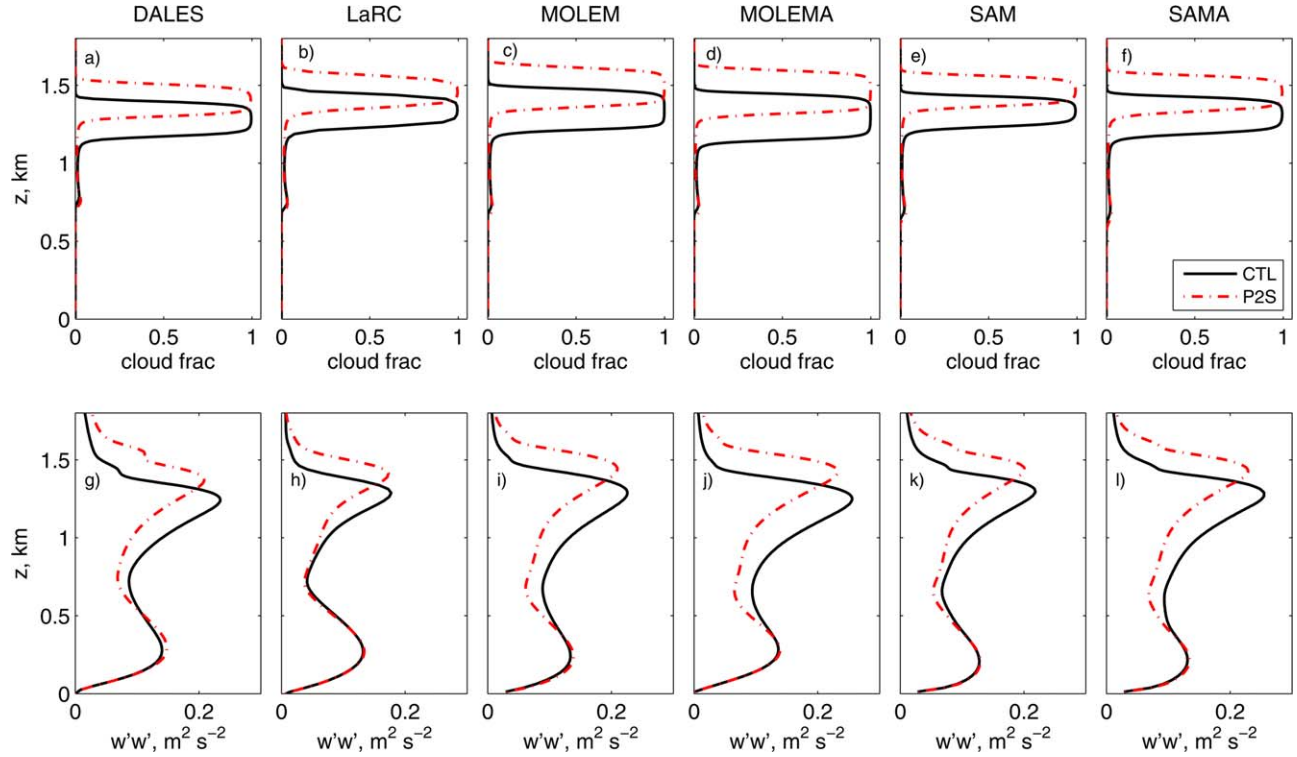

Figure 14. Time-averaged profiles of (a-f) cloud fraction and (g-l) vertical velocity variance for the S11 control and P2S sensitivity studies from the CGILS LES intercomparison are shown from (a,g) DALES, (b,h) LaRC, (c,i) MOLEM, (d,j) MOLEMA, (e,k) SAM, and (f,l) SAMA.

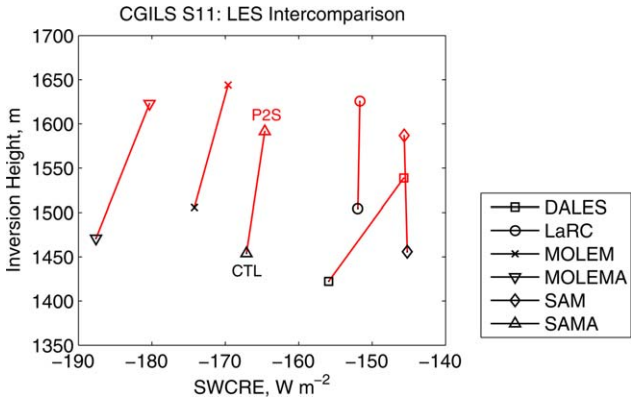

Figure 15. Scatterplot of inversion height (z_i) and SWCRE from the CTL and P2S simulations for the CGILS models at S11. Lines connecting the CTL and P2S simulations from each model emphasize its sensitivity to the climate perturbation.

S12, a mixed-layer approximation cannot be used as an idealization. Perhaps, a bulk formulation with two well-mixed layers in the subcloud and cloud layers separated by a weak inversion at cloud base could give some insight into the mechanisms underlying cloud feedbacks in this case, but we will leave that for future work.

[56] Some of the models (MOLEM, MOLEMA, and LaRC) show weak precipitation at the stratocumulus cloud base that ranges from 0.1 to 0.4 mm d^{-1} (not shown), while the cloud base precipitation rate in the other models is less than 0.1 mm d^{-1}. As the range of cloud changes from CTL to P2S in drizzling and nondrizzling models is similar, precipitation does not seem to explain the difference in cloud changes among the models. In general, one would expect drizzle to act as a governor on the thickening of stratocumulus [e.g., *Ackerman et al.*, 2004], so that the thickening of the cloud with decreased subsidence in the warmer climate would likely be muted in the presence of drizzle. If drizzle was present in both the control and perturbed climate cases, the boundary layer would likely be shallower at equilibrium due to weakened entrainment. It is more difficult to predict the effect of drizzle on climate sensitivity, though it would likely weaken the responses on the thickening side. Note that drizzle would have a larger impact in runs with a diurnal cycle of insolation than those with diurnally averaged insolation, as in the present study.

[57] The steady-state response to combined warming and subsidence changes at S11 is summarized in Figure 15; there is a uniform increase of inversion height in all models, but relatively weak SWCRE change (cloud feedbacks) from −1 to 4 W m^{-2} in four of the six models; the other two models (MOLEMA and DALES) simulated 8 and 10 W m^{-2} SWCRE change due to cloud thinning, respectively. *Bretherton et al.* [2013] show S11 P2 results with the SAMA LES that imply that like in S12, the combined response involves compensation between thermodynamically induced cloud thinning and dynamically induced cloud thickening, though in SAMA the latter is weaker than for S12.

5. S6: Trade Cumulus-Capped Boundary Layer

[58] Figure 16 shows the S6 control (CTL) and perturbed (P2S) thermodynamic reference profiles, subsidence, and horizontal advective forcings. The gradients in the control (ERA monthly-mean) θ and RH profiles between 800 and 870 hPa mark the typical observed range of the trade inversion at S6. Mean subsidence is about half as large as at S11. The perturbed climate forcings are constructed as at the other locations.

[59] Anticipating a cumulus regime rather than the stratocumulus simulated at S11 and S12, the S6 simulations are started cloud-free from the ERA climatological thermodynamic profiles, and the prescribed grid resolution is coarser. This greatly reduces the computational burden compared to S11 or S12, and all models were able to run this case. Because simulations of cumulus convection may be more robust to the advection scheme than simulations of stratocumulus under sharp capping inversions, MOLEM did not run this case with their alternate advection scheme. However, the comparison of SAM and SAMA still tests the sensitivity of the S6 results to the choice of advection scheme.

5.1. S6 Control Simulation

[60] Figure 17 shows S6 time-height plots of cloud fraction for all models. A cumulus cloud layer quickly develops with a cloud base around 500 m. As the cumulus layer deepens, stratocumulus cloud forms at the inversion, with larger fractional cloud cover in some models than others, and drives strengthened entrainment of free-tropospheric air due to cloud-radiation-turbulence feedbacks. The trade inversion rises in response to the strengthened entrainment. In most of the models, the stratocumulus cloud dissipates as the boundary layer deepens, leaving a shallow cumulus boundary layer with little inversion cloud. In WRF and MOLEM, the inversion cloud has not fully dissipated, and the inversion height is still increasing after 10 days, while UCLA settles into a steady state with a little inversion cloud atop the cumulus. The steady-state cumulus layer has a higher cloud fraction in SAM and SAMA than the other models, leading to slightly stronger SWCRE than even the models retaining some inversion cloud. Figure 18 shows that the final values of total water and s_l/c_p in the subcloud and cumulus layers are similar among the models, despite their varying boundary-layer depths (Figure 18) and cloud profiles (Figure 17).

[61] The differences among the model results presumably reflect varying treatments of microphysics, subgrid-scale turbulence, and advection. The effect of advection can be assessed by comparing SAMA to SAM. SAMA initially simulates more stratocumulus than SAM, and the stratocumulus persists up to a higher inversion level, as would be anticipated from its smaller implicit numerical diffusion. However, once the simulations enter the cumulus phase, SAM and SAMA give very similar vertical cloud cover profiles, suggesting the advection scheme is not causing their anomalously large cumulus cloud fraction. The UCLA model has LWPs approximately 50% larger than the other

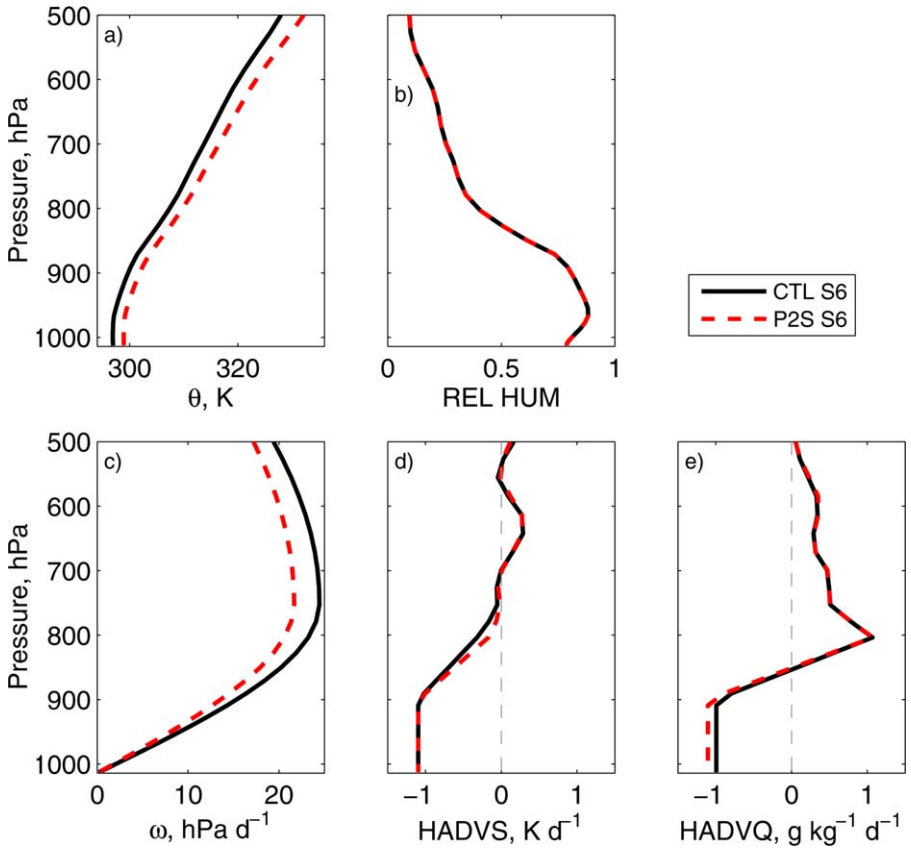

Figure 16. As in Figure 1, but for CGILS S6 control (CTL) and warmed-climate (P2S) simulations. For S6, the runs are initialized with the reference profiles.

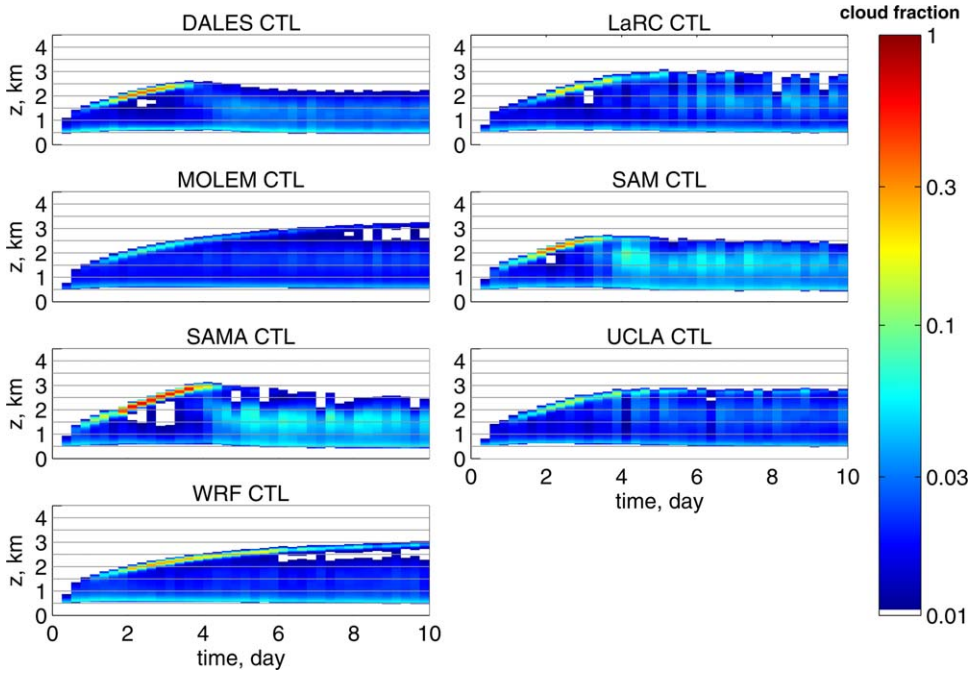

Figure 17. Time-height profiles of cloud fraction for the S6 control simulations in the CGILS LES intercomparison.

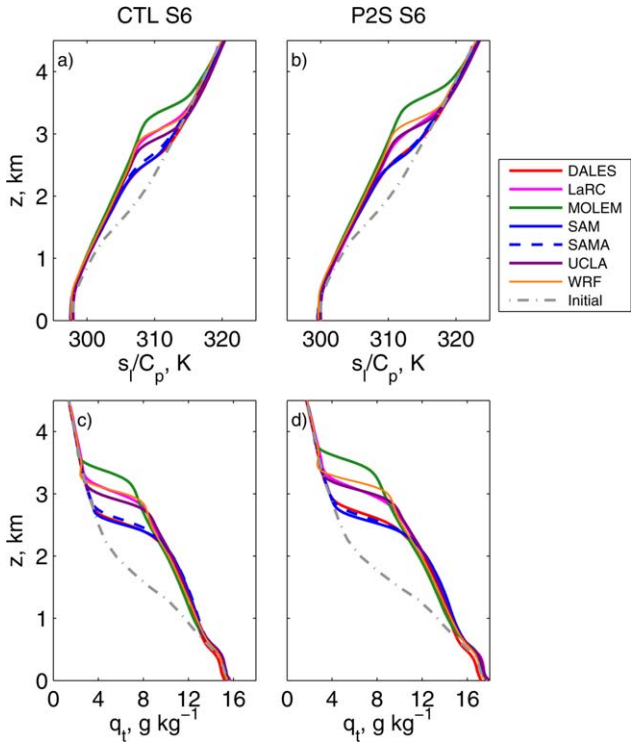

Figure 18. Profiles of (a,b) liquid water static energy divided by c_p and (c,d) total water at the end of the simulations of the S6 (a,c) control and (b,d) P2S sensitivity studies.

models, but its SWCRE is smaller than that of SAM and SAMA (Figure 19 and Table 5). This is likely due to the concentration of liquid water into relatively narrow convective cores in the UCLA simulation and serves as a reminder that the tight relationship between LWP and SWCRE seen in the stratocumulus clouds of S11 and S12 may not hold in the broken cloud fields in S6.

5.1.1. Role of Precipitation in Controlling Inversion Height

[62] The increase of inversion height ceases in most models with the onset of significant surface precipitation, which occurs when cumulus clouds become deep enough to efficiently rain. In Figure 20, 12 h averages of the surface precipitation and entrainment rates are plotted against inversion height and each other, for the CTL and P2S cases. For both cases, the entrainment and precipitation have mirror-image dependence on the inversion height. Early on, the precipitation is low and entrainment strong as the trade inversion height passes through 2000 m. In all the models, the entrainment falls off similarly as the precipitation increases (Figure 20c) in the two cases. In most models, approximately 1 mm d^{-1} of cumulus precipitation reduces entrainment to approximately 3 mm s^{-1} needed to balance mean subsidence in the control simulation (the solid gray curve in Figure 20a) and make a steady state. In WRF, the entrainment rate is anomalously low for a given surface precipitation rate, allowing a steady state with only a 0.5 mm d^{-1} precipitation rate. Precipitation acts to restrain entrainment by removing liquid water from the entrainment zone, making it more difficult to incorporate warm, dry free-tropospheric air into the boundary layer through evaporation, and also inhibiting the formation of inversion cloud that can radiatively drive more entrainment. Energetically, 30 W m^{-2} of latent heating due to approximately 1 mm d^{-1} of precipitation offsets almost half of the radiative and advective cooling of the S6 boundary layer, unlike in S11 and S12, where the radiative and advective cooling of the boundary layer is almost entirely offset by entrainment warming. Thus, we interpret Figure 20c not as an indicator of the cumulus microphysics that create precipitation within each LES, but instead as illustrating the energetic trade-off between precipitation-induced latent heating and entrainment warming of the boundary layer, modulated by model-dependent radiative feedbacks from boundary-layer cloud.

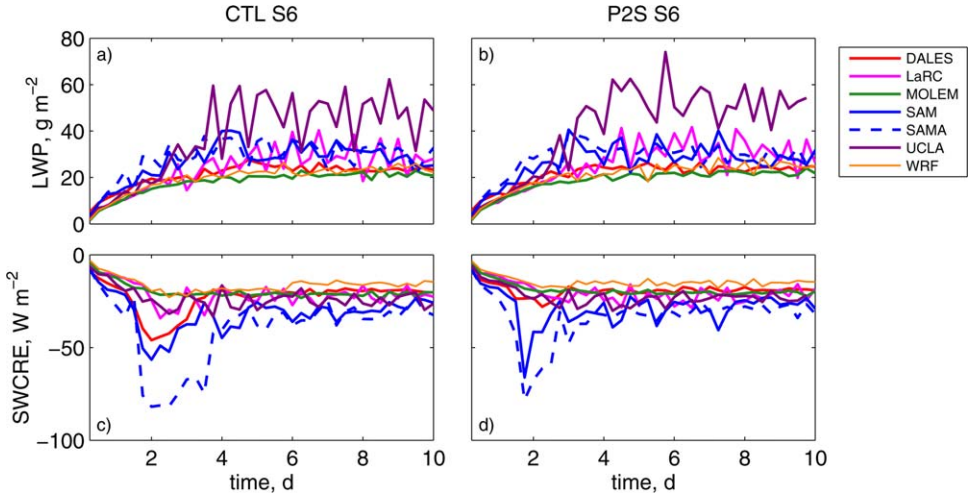

Figure 19. Time series of (a,b) cloud LWP and (c,d) SWCRE for the S6 (a,c) control and (b,d) P2S sensitivity simulations in the CGILS LES intercomparison.

Table 5. Summary of Steady-State (8 to 10 Day Mean) Results for S6[a]

Model	Simulation Name	z_i (m)	z_b (m)	LCL (m)	SHF (W m^{-2})	LHF (W m^{-2})	Prec (mm d^{-1})	CF (%)	LWP (g m^{-2})	SWCRE (W m^{-2})
DALES	CTL	2571	459	527	10.2	122	1.2	17	23	−19
	P2S	2692	462	534	10.1	135	1.5	16	24	−19
LaRC	CTL	3040	486	521	8.2	115	0.9	16	29	−22
	P2S	3110	468	502	8.0	124	1.3	15	30	−21
MOLEM	CTL	3342	532	534	7.5	119	0.8	15	21	−21
	P2S	3514	535	538	6.8	131	1.0	14	22	−20
SAM	CTL	2569	438	469	12.2	115	1.0	21	28	−27
	P2S	2632	432	466	11.8	125	1.2	20	27	−26
SAMA	CTL	2686	427	461	12.4	114	1.1	24	30	−31
	P2S	2688	428	460	11.8	125	1.1	23	29	−29
UCLA	CTL	2953	485	514	8.6	127	1.1	17	49	−25
	P2S	3087	482	509	8.0	137	1.3	16	51	−23
WRF	CTL	3044	488	487	11.3	118	0.4	18	24	−16
	P2S	3175	491	488	11.1	131	0.4	16	25	−15

[a]The averaging time was insufficient to calculate a representative entrainment rate. *Definition of terms:* z_i, inversion height; z_b, cloud base height (computed using same method for stratocumulus cloud base height); LCL, lifting condensation level; w_e, entrainment rate; SHF, sensible heat flux; LHF, latent heat flux; prec, surface precipitation rate; CF, cloud fraction; LWP, liquid water path; SWCRE, shortwave cloud radiative effect.

[63] In SAM, DALES, and LaRC, there is slight hysteresis; the inversion overshoots then falls back down to a steady state due to a collapse in entrainment once the stratocumulus dissipates. In MOLEM and WRF, the entrainment rate decreases less rapidly as the boundary layer deepens and there is no inversion overshoot; UCLA has an intermediate behavior.

5.1.2. Model Biases in Cloud Properties and Vertical Structure

[64] The steady-state inversion heights in the S6 control simulations (2500–3350 m) considerably exceed the summertime climatological averages of cloud top height (1200–1800 m) in *Lin et al*. [2009], and the profiles of s_l/c_p and q_t in all models are correspondingly biased cool and moist compared to ERA between 1200 m and the inversion. As at S11, this bias in inversion height may be related to the simplified CGILS prescription of horizontal advective tendencies. In the S6 control case, the transition from boundary layer to free-tropospheric values of horizontal advective tendencies occurs close to the climatological range of trade inversion heights implied by the ERA RH profile (approximately 800–870 hPa or approximately 1300–2000 m). Once the boundary layer deepens beyond about 850 hPa, the horizontal advective tendency for moisture turns into a source. This was intended to balance subsidence drying in the free troposphere, rather than to moisten a deep cloud layer under the inversion. This effect was noted by *Rieck et al*. [2012], who suggested that it could affect computed climate feedbacks. While it certainly affects the control-state cloud structure, the horizontal advective tendency of humidity turns out to contribute much less to warm-climate perturbations in the moisture budget than do other terms such as increased latent heat flux. An optimistic interpretation is that the simulated S6 cloud feedbacks may be relevant to a location with somewhat warmer SST and a climatologically deeper cumulus layer than at S6, and in any case, they express plausible precipitation-related mechanisms not seen at S11 and S12. We have tested that the boundary-layer deepening can be greatly muted by using a "weak-temperature gradient" feedback between inversion height changes and subsidence rate [*Blossey et al*., 2009], but this was judged too complicated for use in a broad-based LES/SCM intercomparison project and has its own issues of interpretation.

[65] The simulated steady-state LWPs, SWCRE, and cloud fractions (Table 5) are smaller than satellite-derived July climatological averages at S6 [*Lin et al*., 2009; *Xu and Cheng*, 2013], though the latter have uncertainties [*Jones et al*., 2012]. The magnitude of the SWCRE in the models (16–31 W m^{-2}) is also somewhat smaller than the summertime climatological value of approximately 40 W m^{-2} in *Xu and Cheng* [2013].

5.2. S6 Sensitivity to Combined Warming and Subsidence Changes

[66] The broad evolution of the boundary layer in the CTL and P2S simulations for S6 are similar in all models, as seen, for example, in the time-height profiles from DALES (Figure 21). The inversion cloud fraction early in the run is smaller in the DALES P2S run, and the breakup of the inversion cloud occurs almost a day earlier, but these features are not robust across models. Figure 22 shows that the 8 to 10 day mean vertical profiles of boundary-layer cloud fraction and turbulence change remarkably little from CTL to P2S in the models (DALES, SAM/SAMA, and LaRC) in which the inversion cloud fully dissipates and a quasi-steady state has been reached. For the models retaining some inversion cloud (MOLEM, UCLA, and WRF), the 8 to 10 day mean profiles are also very similar, except for a rise of the inversion cloud layer in P2S due to the reduced mean subsidence.

[67] In all models, the CWP and SWCRE have reached statistical steady states in both CTL and P2 after 5 days (Figure 19). The small domain size can only fit one or two evolving cumulus clouds, causing significant high-frequency variability in these statistics in some models, such that a 2 day average is only barely long enough to robustly detect small differences

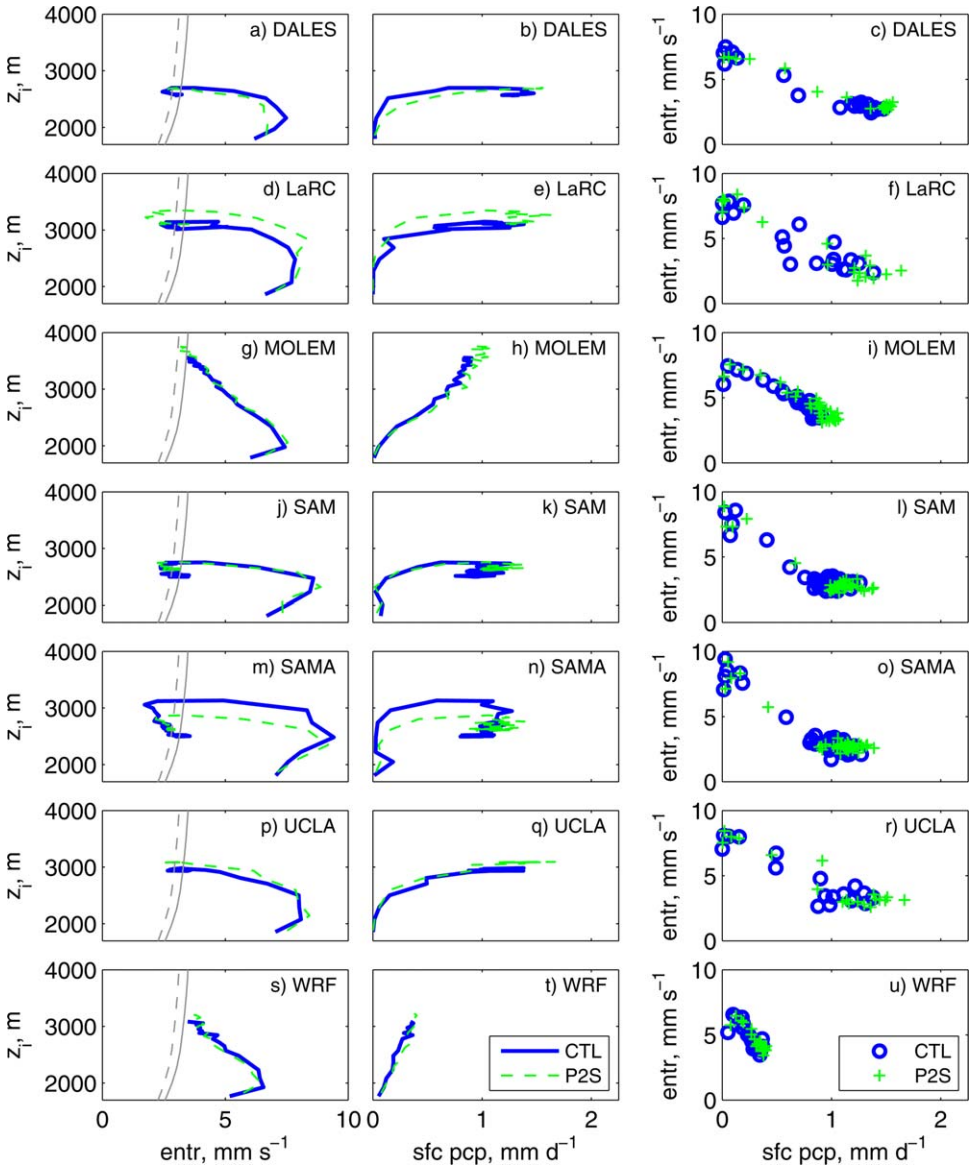

Figure 20. Plots for the S6 CTL and P2S cases of (left) entrainment versus inversion height, (center) surface precipitation rate versus inversion height, and (right) entrainment versus precipitation, for 12 h averaged values from each LES model. In the left column, following *Bretherton et al*. [2010], the solid and dashed gray curves show the mean CTL and P2 subsidence rates at the inversion height; a steady state can be achieved at an inversion height at which entrainment balances subsidence, i.e., where the solid blue curve intersects the solid gray curve for CTL, or where the green dashed curve intersects the dashed gray curve for P2S.

between runs. For SAMA, *Bretherton et al*. [2013] ran both cases out to 20 days; their Table 6 shows 10 to 20 day means of SWCRE for the two runs which reassuringly are the same as our day 8–10 mean values (though this comparison also shows that their steady-state entrainment rates are not adequately sampled by the day 8–10 average, so w_e has been omitted from Table 5). With this caveat about sampling uncertainties, 8 to 10 day mean SWCRE is the same or 1–2 W m^{-2} weaker in P2S than in CTL for all models, suggesting a slight tendency toward positive cloud feedbacks in this regime for the CGILS climate change.

[68] Table 5 shows that in all models, the inversion rises in P2S by 0–170 m (<5%) from CTL, which is much less than suggested by the 11% subsidence decrease. In S6, in contrast to S12 or S11, weaker subsidence in P2S is mainly balanced by less entrainment rather than increases in inversion height. This is a result of entrainment-precipitation feedback: the "precipitation governor" on inversion height noted by *Bretherton et al*. [2013] and studied earlier by *Albrecht* [1993]. The relation between entrainment and precipitation in each model is similar in P2S and CTL (Figure 20). The surface precipitation rate increases in P2S by

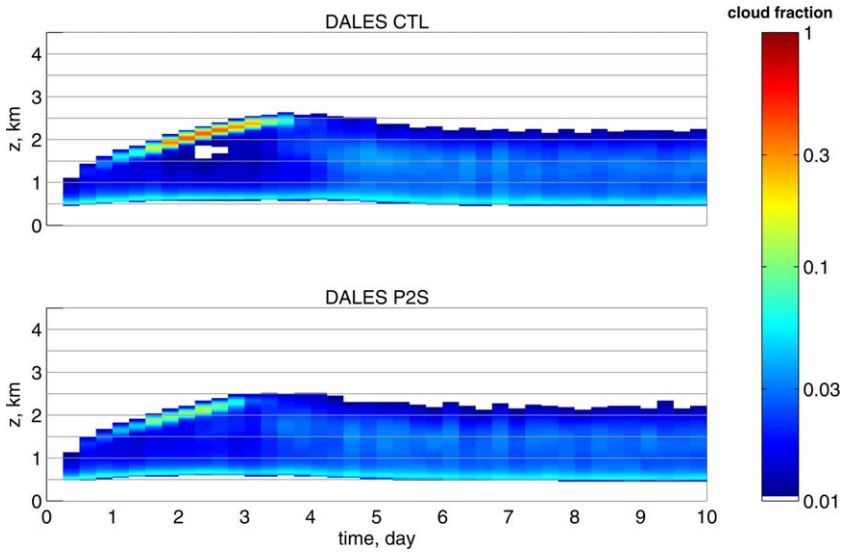

Figure 21. Time-height profiles of cloud fraction for the S6 control and P2S simulations from DALES.

8%–40% in all models, helping suppress entrainment (Figure 20c).

[69] *Wyant et al.* [2009] proposed that stronger boundary-layer clear-sky radiative cooling in a warmer climate could destabilize the trade cumulus boundary layer and lead to *increased* cloudiness. They compared subtropical subsidence regions from control and warm-climate runs of the SP-CAM superparameterized global climate model. In their simulations, the increased specific humidity of the boundary layer in the warmer climate leads to stronger boundary-layer-integrated radiative cooling. The present simulations also have increased boundary-layer-integrated radiative cooling (not shown) due to increased clear-sky longwave cooling, but they do not respond as predicted by *Wyant et al.* [2009]. In the CGILS S6 case, the increased radiative cooling in the perturbed climate is balanced by increased precipitation, rather than by increased

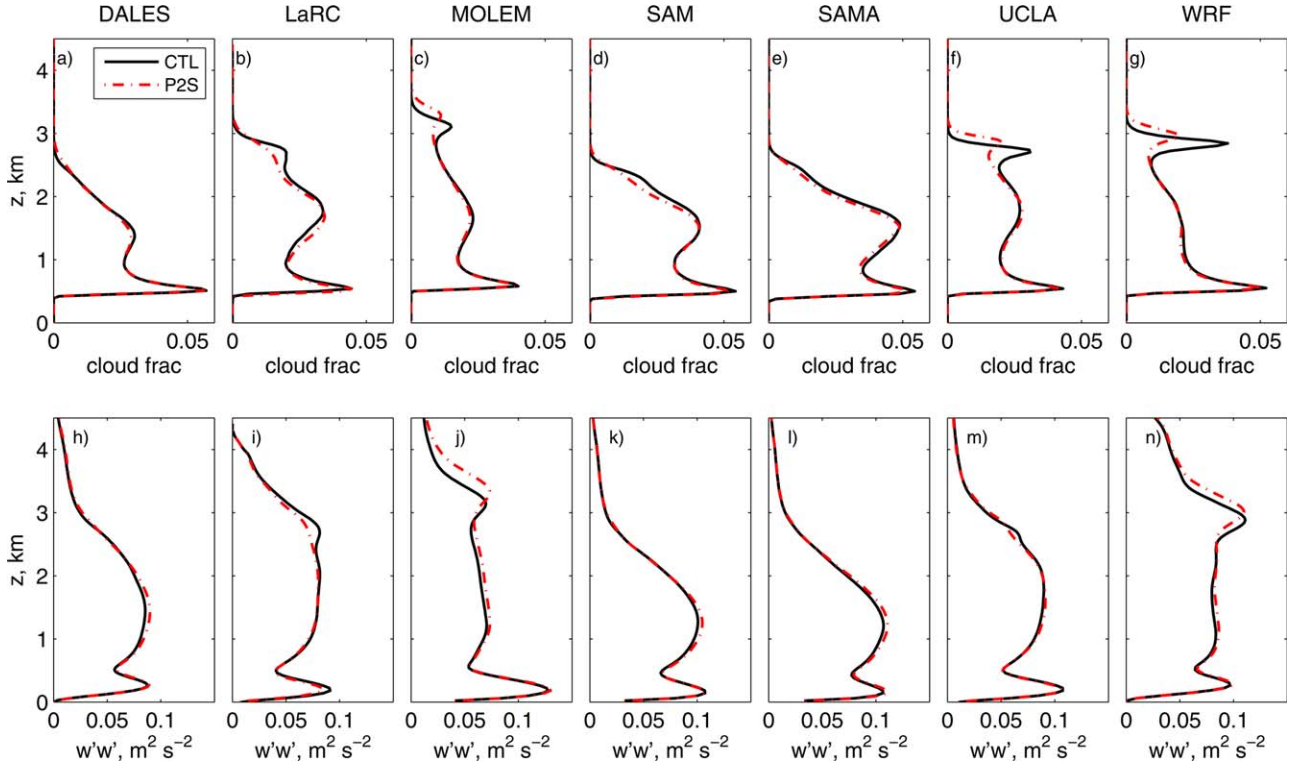

Figure 22. Time-averaged profiles of (a-g) cloud fraction and (h-n) vertical velocity variance for the S6 control and P2S sensitivity studies from the CGILS LES intercomparison are shown from (a,h) DALES, (b,i) LaRC, (c,j) MOLEM, (d,k) SAM, (e,l) SAMA, (f,m) UCLA, and (g,n) WRF.

entrainment warming in LES simulations by *Blossey et al*. [2009], the companion paper to *Wyant et al*. [2009]. Those simulations also found increased inversion stability in the perturbed climate, and most of the cloud increases occurred close to the inversion in the LES runs. In the coarse resolution CRM runs, increases in cloudiness occurred through most of the cloud layer. While the clear-sky radiative cooling of the boundary layer is stronger in the warmer climate in all three CGILS cases, S12, S11, and S6, the overcast conditions at S12 and S11 lead the full sky radiative cooling to be weaker at those locations.

6. Discussion and Conclusions

[70] The sensitivity of marine boundary-layer clouds to idealized climate changes has been explored in six LES models as part of the CGILS LES intercomparison. The models agree well on the structure of the cloud-topped boundary layer in the control climate and on its response to the CGILS-specified climate change, with somewhat more variability among models at the S6 trade cumulus where precipitation plays a significant role.

[71] In the fully overcast (S11 and S12) cases, the inversion height increases in all the models due to decreased subsidence. The simulated cloud changes are of uncertain sign, though most models show negative feedbacks for the well-mixed stratocumulus layer simulated over the cold-SST location S12, and all models produce neutral or positive feedbacks for the cumulus-under-overcast-stratocumulus layer simulated over the cool-SST location S11. For S12, an additional simulation was performed to separate the effects of the thermodynamic (warming) and the dynamic (subsidence) components of the climate change. All models respond similarly, with thinning in response to the warming, and boundary-layer deepening, cloud thickening, and some decoupling when the subsidence is reduced. The model dependence of the overall cloud response at both S12 and S11 is interpreted as due to differing degrees of compensation between these mechanisms in different LESs, primarily due to their advection and subgrid turbulence schemes. The companion paper, *Bretherton et al*. [2013], uses a single LES to analyze in detail and describe the mechanisms inducing these cloud sensitivities.

[72] At the warm-SST location S6, the models correctly simulate a trade cumulus boundary layer. As at S11, the trade inversion is much higher than observed, suggesting shortcomings in the specification of the forcings, in particular the horizontal advective tendencies. As a result, the onset of cumulus precipitation plays an important role in regulating the height of the simulated trade inversion by suppressing entrainment deepening. In the warmer climate with reduced subsidence, precipitation increases, entrainment decreases, and the inversion heights rise only slightly in all models. All models produce neutral to slightly positive cloud feedbacks in the warmer climate due to very slight decreases in cloud fraction. As precipitation plays a role in the response of the boundary layer to climate perturbations, the cloud response to climate perturbations in nonprecipitating trade cumulus boundary layers might differ from that found here.

[73] The S6 case is marked by relatively larger differences in boundary-layer structure among the models. One likely contributor is differences in LES microphysical parameterizations [*Stevens and Seifert*, 2008]. As the transition from stratocumulus-capped to trade wind cumulus boundary layers may be influenced by precipitation and aerosol, there is a need to further develop and validate robust bulk microphysics schemes that perform well across the full range of boundary-layer cloud types, not to mention deep convection and other higher-topped clouds.

[74] The broad agreement among the models in simulating three key subtropical marine boundary-layer cloud regimes and their sensitivity to an idealized climate perturbations suggests that further studies with individual LES models focusing on other basic climate scenarios or other climate-related forcing changes may give representative results, as in the companion paper by *Bretherton et al*. [2013]. However, partial compensation of opposing responses to the thermodynamic and dynamic components of the CGILS idealized climate change led to model dependence of even the sign of the implied cloud feedback at the two stratocumulus locations, even though the two components individually produce cloud responses of consistent sign among models.

[75] Two lessons are that (1) LES-predicted cloud response is sensitive to details of the imposed climate forcing perturbation, and oversimplifying the forcing perturbation may give misleading results, and (2) if there are compensating responses to different elements of a realistic climate perturbation, that will greatly increase the relative uncertainty in a net cloud feedback strength predicted by any model, including an LES. Hence, we should be circumspect about how precisely the problem of low cloud feedback on climate can be understood using a bottom-up reductionist approach; observational constraints at global and process-level scales will also have to play a central role, not just in improving models but in accurately and comprehensively documenting large-scale cloud responses to climate variability and change. However, we have demonstrated promise for using LES as a benchmark for testing the realism of the response of SCMs to carefully chosen climate perturbations.

[76] The LES component of CGILS has been an ambitious model intercomparison project. The agreement among the models came only after careful analysis of early simulations that rooted out errors, inconsistencies, and ambiguities in implementing the forcings and after adding specifications that further constrained the LES surface flux and radiation parameterizations.

[77] Much of the overall initial design of the CGILS intercomparison was by necessity frozen near its inception. Future studies of marine boundary-layer cloud

response to climate perturbations in a single-column study might benefit from a careful consideration of the CGILS framework and how it might be improved. Intercomparison of model sensitivity to a CO_2 change and a change in LTS would test the robustness of single-LES sensitivity studies that have looked at these issues [e.g., *Bretherton et al*., 2013]. The specification of horizontal advective forcings in CGILS clearly led to serious artificial boundary-layer deepening for the S6 and S11 cases. This might be reduced by a more careful approach to blending boundary-layer and free-tropospheric advective tendencies according to a climatological range of inversion heights, rather than the CGILS approach of using an arbitrary range of heights. In studies using one or just a few models, the horizontal advective profiles or vertical motion profile could adapt to a diagnosed trade inversion height in the model with boundary-layer advective forcings applied below that height and free-tropospheric ones above. For comparison with SCMs and observations, it would be desirable to use forcings with realistic time dependence [*Brient and Bony*, 2012; Zhang et al. [2012]. This may now be computationally feasible for some LES models, particularly for the S6 case. It is also feasible to add diurnally varying insolation or at a minimum use a more accurate insolation-weighted solar zenith angle [see *Bretherton et al*., 2013; *Hartmann*, 1994, chap. 2]. We anticipate that the next LES phase of CGILS will explore several of these issues and lead to further improvement in our ability to understand and simulate low cloud feedbacks on climate.

Appendix: A

Additional LES Case Specifications for CGILS

[78] The design and derivation of the forcings for the CGILS cases is described by *Zhang et al*. [2012]. Here the specific ways in which the forcings have been applied in and adapted to the LES models are described.

A1. Lower Minimum Heights for Thermodynamic Nudging

[79] Small differences in radiative heating rates among the models above the inversion can lead to large intermodel differences in the free-tropospheric temperature and LTS over the course of multiday simulations. To mitigate possible impacts of such drifts, temperature and humidity were nudged toward their reference profiles. For the CGILS SCMs, nudging was used at pressures below 600 hPa for all three cases. With this specification, free-tropospheric drift was still an important cause of differences between the boundary-layer cloud profiles simulated by the LES models in cases S11 and S12, so the bottom of the nudging layer was lowered. As noted in Table 1, the nudging rate γ_{nudge} varies with height as

$$\gamma_{\mathrm{nudge}} = \begin{cases} 0 & z < z_{\mathrm{relax}} \\ \frac{1}{2}\tau_{\mathrm{nudge}}^{-1}\left(1-\cos\left(\pi\frac{z-z_{\mathrm{relax}}}{z_{\mathrm{relax}}^{+}-z_{\mathrm{relax}}}\right)\right) & z_{\mathrm{relax}} < z < z_{\mathrm{relax}}^{+} \\ \tau_{\mathrm{nudge}}^{-1} & z > z_{\mathrm{relax}}^{+} \end{cases}.$$

[80] For the three cases, S12, S11, and S6, z_{relax} has the values 1200, 2500, and 4000 m, respectively, while z_{relax}^{+} has the values 1500, 3000, and 4800 m.

A2. Harmonization of Cloud Droplet Number Concentration, Effective Radius, and Radiative Transfer Scheme

[81] The differences in the simulated free-tropospheric temperature profiles also led to an effort to harmonize the radiative parameterizations of the models. As a result, some models adopted an LES interface developed by the lead author to the Rapid Radiative Transfer Model for Global climate model applications (RRTMG) radiation scheme. Varying assumptions about cloud droplet effective radius led models with similar cloud LWPs and cloud fractions to have quite different albedos. To ensure that the models had a similar relationship among cloud LWP, cloud fraction, and cloud albedo, the cloud droplet effective radius was parameterized in all models using the relationship adopted in the LES transition cases [*de Roode et al*., 2012] and described below.

[82] In CGILS, a cloud droplet concentration $N_c = 100\ \mathrm{cm}^{-3}$ was specified for the microphysical parameterizations. For the LES models, the cloud droplet effective radius r_{eff} input into the radiation scheme was computed based on the volume-mean radius r_v and an assumed log-normal cloud droplet size distribution with a geometric standard deviation $\sigma_g = 1.2$ [*Ackerman et al*., 2009] as $r_{\mathrm{eff}} = r_v \exp\left(\ln\left(\sigma_g\right)^2\right)$. The volume-mean radius was calculated as

$$r_v = \left(\frac{3\rho_{\mathrm{air}} q_c}{4\pi\rho_{\mathrm{liq}} N_d}\right)^{1/3}. \quad \text{(A1)}$$

[83] Here q_c is cloud liquid water mass mixing ratio, and ρ_{air} and ρ_{liq} are the densities of dry air and liquid water, respectively.

A3. Uniform Bulk Surface Flux Scheme and Wind Nudging

[84] Strong nudging of the mean wind profile (on a 10 min timescale) was adopted to produce a consistent surface wind speed, which the individual models would use in computing surface sensible and latent heat fluxes. Unfortunately, differences in the parameterization of subgrid stresses among the LES models near the surface still led to differences in wind speeds and surface fluxes that affected the simulated clouds.

[85] Hence, all LES models adopted a simplified surface flux formula for scalars:

$$w's' = c_T\left(c_p \mathrm{SST} - s_1\right), \tag{A2}$$

$$w'q' = c_T(0.98 q_{\mathrm{sat}}(P_s, \mathrm{SST}) - q_1), \tag{A3}$$

where s_1 and q_1 are values of dry static energy and q_v at the lowest model level, $q_{\mathrm{sat}}(P_s, \mathrm{SST})$ is the saturation specific humidity at the surface pressure and SST, and

$$c_T = c_q U_{\mathrm{spd}} \left\{\frac{\ln(10/z_0)}{\ln(z_1/z_0)}\right\}^2, \tag{A4}$$

where U_{spd} is the 10 m surface wind speed, $c_q = 1.2\times10^{-3}$ is a nondimensional bulk transfer coefficient, and the final term is a neutral-stratification log-layer correction factor based on the height z_1 in meters of the lowest model level and an assumed surface momentum and scalar roughness length $z_0 = 10^{-4}$ m. The values of c_T used and the assumed z_1 on which they are based are given in Table 1. They are based on the surface wind speeds specified in *Zhang et al*. [2012, Table 1], but for historical reasons the S6 and S11 values were adjusted down and up approximately 3%, respectively, to be equal to each other. *Bretherton et al*. [2013] consider the sensitivity of cloud at the three CGILS locations to wind speed changes by changing U_{spd} in equation (A4).

[86] This scheme was not used for momentum fluxes, which were computed by each LES using its default surface drag parameterization. To try to mimic the structure of an SCM and minimize transients due to damped inertial oscillations, only profile relaxation, not geostrophic (large-scale pressure gradient) forcing, was applied to the winds at all levels.

A4. Moisture Floor in S12

[87] The CGILS forcings were designed for easy application across a number of single-column and LES models. This included a simple specification of the vertical profile of large-scale horizontal advection, with dry and cold advection applied uniformly up to 900 hPa and horizontal advective tendencies above 800 hPa that balanced the free-tropospheric moisture and energy budgets under clear-sky conditions. The advective tendencies between 800 and 900 hPa were interpolated between these two tendencies. In S12, the LES-simulated inversion pressure exceeded 900 hPa, so dry and cold advection characteristic of the boundary layer was applied to free-tropospheric air above the inversion, creating an unrealistic local humidity minimum just above the inversion that leads to excessive entrainment drying of the boundary layer. To prevent this, when the mean humidity at any layer below 1.3 km dropped below a moisture floor equal to the reference humidity at 1.3 km, it was nudged back to the floor on a timescale of 1 h. The same issue affected the early transient evolution of the S11 simulations, but the steady-state behavior was not strongly affected, and the computational expense of rerunning the case was judged too large to add a moisture floor for S11.

A5. Modification of Subsidence in S12

[88] In simulations of the S12 case with the CGILS-specified vertical motion profile, which had a surface divergence rate 5.60×10^{-6} s^{-1}, the strong subsidence gradually forced the inversion to fall below the LCL and lead to the dissipation of the stratocumulus cloud in most of the LES models. The vertical motion profile was rescaled to slightly reduce the surface divergence rate to 5.25×10^{-6} s^{-1} (a reduction within the range consistent with ERA and surface divergence data sets), so that all models could obtain a steady state. Together with the moisture floor above the inversion, this led to robust simulations of a well-mixed stratocumulus-capped boundary layer across the models. The horizontal advective tendencies above 800 hPa were slightly adjusted to balance the reduced subsidence heating and drying aloft.

Appendix: B

LES Models

[89] The LES models used in this study are detailed in the following paragraphs. Unless otherwise mentioned, the models use liquid water potential temperature, two moment bulk microphysical representations of precipitating water (rain/drizzle), and monotonic advection schemes for scalar quantities and compute radiative fluxes and heating rates using RRTMG [*Iacono et al*., 2008]. An interface to RRTMG was added to many of these models during the course of this project.

B1. SAM

[90] The System for Atmospheric Modeling (SAM), version 6.7.5, is described in detail by *Khairoutdinov and Randall* [2003]. The present simulations include the microphysics of *Khairoutdinov and Kogan* [2000]. The advection scheme in the SAMA simulations is based on *Blossey and Durran* [2008], rather than the default scheme of *Smolarkiewicz and Grabowski* [1990]. As opposed to the other models in this study, SAM uses liquid static energy as a prognostic variable, rather than liquid water potential temperature.

B2. DALES

[91] The Dutch Atmospheric Large Eddy Simulation (DALES) model is described in detail by *Heus et al*. [2010]. DALES is distinct from the other models (except WRF) in that flux-limiting/slope-limiting advection schemes are not used for the scalar fields.

B3. MOLEM

[92] The Met Office Large Eddy Model (MOLEM) is configured as described by *Ackerman et al*. [2009],

except that fully interactive radiation is used and advection of momentum fields uses centered, rather than monotonic advection. In MOLEMA, monotonic advection [*Leonard et al*., 1993] is used for all fields, including momentum. MOLEM advects potential temperature, water vapor, and cloud liquid, rather than liquid water potential temperature and total water. All MOLEM simulations at S12 nudge the local wind field back to the background profiles from 50 m above the inversion and nudge the domain mean wind below that level. The nudging of the local wind field above the inversion prevents oscillations in the free troposphere that were encountered in some simulations of S12 with MOLEM and affected the evolution of the cloud field.

B4. UCLA

[93] The University of California Los Angeles (UCLA) LES model used in the present simulations is described by *Savic-Jovcic and Stevens* [2008]. Radiative heating is computed using the recently developed Monte Carlo spectral integration technique [*Pincus and Stevens*, 2009]. The microphysical parameterization is based on *Seifert and Beheng* [2001, 2006].

B5. LaRC

[94] The NASA Langley Research Center (LaRC) used an early version (1.1) of the UCLA LES model, using RRTMG for radiative heating computations. As the treatment of time integration, advection, microphysics, and radiation have changed in the UCLA model over time, the models used in the LaRC and UCLA simulations can be thought of as cousins. Due to computational constraints, LaRC's simulations of S11 and S12 used coarser vertical resolution than the other models, with Δz in the inversion zone of 25 m in S11 and 7.5 m in S12.

B6. WRF

[95] The Advanced Research version of Weather Research and Forecasting (WRF-ARW) model is described by *Skamarock et al*. [2008]. The present simulations use WRF-FASTER that is a framework developed in the FAst-physics System TEstbed and Research (FASTER) project to enable flexible configurations for vertical grid spacing and forcings, among others. WRF uses potential temperature as a prognostic variable. The simulations employ a third-order Runge-Kutta time integration with a fifth- and third-order spatial discretization for horizontal and vertical advections, respectively. A positive-definite limiter is further applied to all scalar advections. Radiative transfer is calculated by RRTMG and the interface designated for this project, rather than the simple version originally implemented in WRF. Microphysics is simulated by the one-moment Purdue-Lin scheme [*Lin et al*., 1983], modified to incorporate cloud water sedimentation.

[96] **Acknowledgments.** Blossey and Bretherton acknowledge support from the Center for Multiscale Modeling and Prediction (CMMAP), supported by NSF. The authors also thank Marat Khairoutdinov of Stony Brook University for his sustained leadership in maintaining SAM, Matthew Wyant for providing Figure 5, and Andy Ackerman for proposing the approach for computing effective radius. De Roode is supported through the European Union Cloud Intercomparison, Process Study & Evaluation Project (EUCLIPSE), funded under Framework Program 7 of the European Union. Heus was funded by the Deutscher Wetter Dienst (DWD) through the Hans-Ertel Centre for Weather Research. The simulations with the Dutch LES model were sponsored by the National Computing Facilities Foundation (NCF). Endo, Liu, and Zhang were supported by the U.S. Department of Energy (DOE) Earth System Modeling (ESM) program through the FASTER project (www.bnl.gov/esm). Zhang was also supported by the NASA Modeling and Analysis Program (MAP) and the U.S. National Science Foundation. The authors would also like to thank two anonymous referees for their comments.

References

Ackerman, A.S., M.P. Kirkpatrick, D.E. Stevens, and O.B. Toon (2004), The impact of humidity above stratiform clouds on indirect aerosol climate forcing, *Nature*, *432*, 1014–1017, doi:10.1038/nature03174.

Ackerman, A.S., et al. (2009), Large-eddy simulations of a drizzling, stratocumulus-topped marine boundary layer, *Mon. Weather Rev.*, *137*, 1083–1110, doi:10.1175/2008MWR2582.1.

Albrecht, B.A. (1993), Effects of precipitation on the thermodynamic structure of the trade wind boundary layer, *J. Geophys. Res.*, *98*(D4), 7327–7337, doi:10.1029/93JD00027.

Andrews, T., J.M. Gregory, M.J. Webb, and K.E. Taylor (2012), Forcing, feedbacks and climate sensitivity in CMIP5 coupled atmosphere-ocean climate models, *Geophys. Res. Lett.*, *39*, L09712, doi:10.1029/2012GL051607.

Berner, A.H., C.S. Bretherton, and R. Wood (2011), Large-eddy simulation of mesoscale dynamics and entrainment around a pocket of open cells observed in VOCALS-REx RF06, *Atmos. Chem. Phys.*, *11*, 10,525–10,540, doi:10.5194/acp-11–10525-2011.

Blossey, P.N., and D.R. Durran (2008), Selective monotonicity preservation in scalar advection, *J. Comput. Phys.*, *227*(10), 5160–5183, doi:10.1016/j.jcp.2008.01.043.

Blossey, P.N., C.S. Bretherton, and M.C. Wyant (2009), Subtropical low cloud response to a warmer climate in an superparameterized climate model. Part II: Column modeling with a cloud resolving model, *J. Adv. Model. Earth Syst.*, *1*, 14 pp., doi:10.3894/JAMES.2009.1.8.

Bony, S., and J. Dufresne (2005), Marine boundary layer clouds at the heart of tropical cloud feedback uncertainties in climate models, *Geophys. Res. Lett.*, *32*, L20806, doi:10.1029/2005GL023851.

Bony, S., J.-L. Dufresne, H.L. Treut, J.-J. Morcrette, and C. Senior (2004), On dynamic and thermodynamic components of cloud changes, *Clim. Dyn.*, *22*(2–3), 71–86, doi:10.1007/s00382-003-0369-6.

Bretherton, C.S., et al. (1999), An intercomparison of radiatively driven entrainment and turbulence in a smoke cloud, as simulated by different numerical models, *Q.J. R. Meteorol. Soc.*, *125*(554), 391–423.

Bretherton, C.S., J. Uchida, and P.N. Blossey (2010), Slow manifolds and multiple equilibria in stratocumulus-capped boundary layers, *J. Adv. Model. Earth Syst.*, *2*, 20 pp., doi:10.3894/JAMES.2010.2.14.

Bretherton, C.S., P.N. Blossey, and C. Jones (2013), Mechanisms of marine low cloud sensitivity to idealized climate perturbations: A single-LES exploration extending the CGILS cases, *J. Adv. Model. Earth Syst.*, doi:10.1002/jame.20019, in press.

Brient, F., and S. Bony (2012), Interpretation of the positive low-cloud feedback predicted by a climate model under global warming, *Clim. Dyn.*, 1–17, doi:10.1007/s00382-011-1279-7.

Caldwell, P., and C.S. Bretherton (2009), Large eddy simulation of the diurnal cycle in southeast Pacific stratocumulus, *J. Atmos. Sci.*, *66*, 432–449, doi:10.1175/2008JAS2785.1.

Caldwell, P.M., Y. Zhang, and S.A. Klein (2012), CMIP3 subtropical stratocumulus cloud feedback interpreted through a mixed-layer model, *J. Clim.*, *26*, 1607–1625, doi:10.1175/JCLI-D-12–00188.1.

Cheng, A., K.-M. Xu, and B. Stevens (2010), Effects of resolution on the simulation of boundary-layer clouds and the partition of kinetic energy to subgrid scales, *J. Adv. Model. Earth Syst.*, *2*, 21 pp., doi:10.3894/JAMES.2010.2.3.

de Roode, S.R., I. Sandu, J.J. van der Dussen, A.S. Ackerman, P.N. Blossey, A. Lock, A.P. Siebesma, and B. Stevens (2012), LES results

of the GASS-EUCLIPSE Lagrangian stratocumulus to shallow cumulus transition cases, in *20th Symposium on Boundary Layers and Turbulence*, *Am. Meteorol. Soc.*

Dee, D.P., et al. (2011), The ERA-Interim reanalysis: Configuration and performance of the data assimilation system, *Q.J. R. Meteorol. Soc.*, *137*, 553–597, doi:10.1002/qj.828.

Hartmann, D.L. (1994), *Global Physical Climatology*, 411 pp., Academic, San Diego, Calif.

Heus, T., et al. (2010), Formulation of the Dutch Atmospheric Large-Eddy Simulation (DALES) and overview of its applications, *Geosci. Model Dev.*, *3(2)*, 415–444, doi:10.5194/gmd-3–415-2010.

Iacono, M.J., J. Delamere, E. Mlawer, M. Shephard, S. Clough, and W. Collins (2008), Radiative forcing by long-lived greenhouse gases: Calculations with the AER radiative transfer models, *J. Geophys. Res.*, *113*, D13103, doi:10.1029/2008JD009944.

Jones, A.L., L. DiGirolamo, and G. Zhao (2012), Reducing the resolution bias in cloud fraction from satellite derived clear-conservative cloud masks, *J. Geophys. Res.*, *117*, D12201, doi:10.1029/2011JD017195.

Khairoutdinov, M.F., and Y. Kogan (2000), A new cloud physics parameterization in a large-eddy simulation model of marine stratocumulus, *Mon. Weather Rev.*, *128*, 229–243.

Khairoutdinov, M.F., and D.A. Randall (2003), Cloud resolving modeling of the ARM summer 1997 IOP: Model formulation, results, uncertainties, and sensitivities, *J. Atmos. Sci.*, *60*, 607–625, doi:10.1175/1520-0469(2003)060<0607:CRMOTA>2.0.CO;2.

Klein, S.A., and D.L. Hartmann (1993), The seasonal cycle of low stratiform clouds, *J. Clim.*, *6*, 1587–1606, doi:10.1175/1520-0442(1993)006<1587:TSCOLS>2.0.CO;2.

Klein, S.A., Y. Zhang, M.D. Zelinka, R. Pincus, J. Boyle, and P.J. Gleckler (2012), Are climate model simulations of clouds improving? An evaluation using the ISCCP simulator, *J. Geophys. Res.*, 118, doi:10.1002/jgrd.50141.

Leonard, B.P., M.K. MacVean, and A.P. Lock (1993), Positivity-preserving numerical schemes for multidimensional advection, Tech. Rep., Tech. Memo. 106055, ICOMP-93-05, NASA.

Lin, W., M. Zhang, and N.G. Loeb (2009), Seasonal variation of the physical properties of marine boundary layer clouds off the California coast, *J. Clim.*, *22*, 2624–2638, doi:10.1175/2008JCLI2478.1.

Lin, Y.-L., R.D. Farley, and H.D. Orville (1983), Bulk parameterization of the snow field in a cloud model, *J. Clim. Appl. Meteorol.*, *22*, 1065–1092, doi:10.1175/1520-0450(1983)022<1065:BPOTSF>2.0.CO;2.

Pincus, R., and B. Stevens (2009), Monte Carlo spectral integration: a consistent approximation for radiative transfer in large eddy simulations, *J. Adv. Model. Earth Syst.*, *1*, 9 pp., doi:10.3894/JAMES.2009.1.1.

Rieck, M., L. Nuijens, and B. Stevens (2012), Marine boundary-layer cloud feedbacks in a constant relative humidity atmosphere, *J. Atmos. Sci.*, *69*, 2538–2550, doi:10.1175/JAS-D-11–0203.1.

Sandu, I., and B. Stevens (2011), On the factors modulating the stratocumulus to cumulus transitions, *J. Atmos. Sci.*, *68*, 1865–1881, doi:10.1175/2011JAS3614.1.

Savic-Jovcic, V., and B. Stevens (2008), The structure and mesoscale organization of precipitating stratocumulus, *J. Atmos. Sci.*, *65*, 1587–1605, doi:10.1175/2007JAS2456.1.

Seifert, A., and K.D. Beheng (2001), A double-moment parameterization for simulating autoconversion, accretion and selfcollection, *Atmos. Res.*, 59–60, 265–281, doi:10.1016/S0169–8095(01)00126-0.

Seifert, A., and K.D. Beheng (2006), A two-moment cloud microphysics parameterization for mixed-phase clouds. Part 1: Model description, *Meteorol. Atmos. Phys.*, *92*, 45–66, doi:10.1007/s00703-005-0112-4.

Skamarock, W.C., J.B. Klemp, J. Dudhia, D.O. Gill, D.M. Barker, M. Duda, H. Huang, W. Wang, and J.G. Powers (2008), A description of the Advanced Research WRF version 3, Tech. Rep., Tech. Note NCAR/TN-475+STR, NCAR, 113 pp.

Smolarkiewicz, P.K., and W.W. Grabowski (1990), The multi-dimensional positive definite advection transport algorithm: Non-oscillatory option, *J. Comput. Phys*, *86*, 355–375, doi:10.1016/0021–9991(90)90105-A.

Soden, B.J., and I.M. Held (2006), An assessment of climate feedbacks in coupled ocean–atmosphere models, *J. Clim.*, *19*, 3354–3360, doi:10.1175/JCLI3799.1.

Soden, B.J., and G.A. Vecchi (2011), The vertical distribution of cloud feedback in coupled ocean-atmosphere models, *Geophys. Res. Lett.*, *38*, L12704, doi:10.1029/2011GL047632.

Somerville, R.C.J., and L.A. Remer (1984), Cloud optical thickness feedbacks in the CO2 climate problem, *J. Geophys. Res.*, *89*(D6), 9668–9672, doi:10.1029/JD089iD06p09668.

Stevens, B., and A. Seifert (2008), Understanding macrophysical outcomes of microphysical choices in simulations of shallow cumulus convection, *J. Meteorol. Soc. Jpn.*, *86A*, 143–162, doi:10.2151/jmsj.86A.143.

Stevens, B., et al. (1995), Evaluation of large-eddy simulations via observations of nocturnal marine stratocumulus, *Mon. Weather Rev.*, *133*, 1443–1462, doi:10.1175/MWR2930.1.

Teixeira, J., et al. (2011), Tropical and subtropical cloud transitions in weather and climate prediction models: The GCSS/WGNE Pacific Cross-Section Intercomparison (GPCI), *J. Clim.*, *24*, 5223–5256, doi:10.1175/2011JCLI3672.1.

Turton, J.D., and S. Nicholls (1987), A study of the diurnal variation of stratocumulus using a multiple mixed layer model, *Q.J. R. Meteorol. Soc.*, *113*, 969–1009, doi:10.1002/qj.49711347712.

vanZanten, M.C., et al. (2011), Controls on precipitation and cloudiness in simulations of trade-wind cumulus as observed during RICO, *J. Adv. Model. Earth Syst.*, *3*, M06001, doi:10.1029/2011MS000056.

Vecchi, G.A., and B.J. Soden (2007), Global warming and the weakening of the tropical circulation, *J. Clim.*, *20*, 4316–4340, doi:10.1175/JCLI4258.1.

Webb, M., F. Lambert, and J. Gregory (2012), Origins of differences in climate sensitivity, forcing and feedback in climate models, *Clim. Dyn.*, 1–31, doi:10.1007/s00382-012-1336-x.

Wood, R., and C.S. Bretherton (2006), On the relationship between stratiform low cloud cover and lower-tropospheric stability, *J. Clim.*, *19*, 6425–6432, doi:10.1175/JCLI3988.1.

Wyant, M.C., C.S. Bretherton, and P.N. Blossey (2009), Subtropical low cloud response to a warmer climate in an superparameterized climate model. Part I: Regime sorting and physical mechanisms, *J. Adv. Model. Earth Syst.*, *1*, 11 pp., doi:10.3894/JAMES.2009.1.7.

Xu, K.-M., and A. Cheng (2013), Improving low-cloud simulation with an upgraded multiscale modeling framework. Part II: Seasonal variations over the eastern Pacific, *J. Clim.*, doi:10.1175/JCLI-D-12–00276.1, in press.

Xu, K.-M., A. Cheng, and M. Zhang (2010), Cloud-resolving simulation of low-cloud feedback to an increase in sea surface temperature, *J. Atmos. Sci.*, *67*, 730–748, doi:10.1175/2009JAS3239.1.

Zhang, M., C. Bretherton, P. Blossey, S. Bony, F. Brient, and C. Golaz (2012), An experimental design to investigate low cloud feedbacks in general circulation models for CGILS by using single-column and large-eddy models, *J. Adv. Model. Earth Syst.*, 4, M12001, doi:10.1029/2012MS000182.

Zhang, M.-H., and C.S. Bretherton (2008), Mechanisms of low cloud–climate feedback in idealized single-column simulations with the Community Atmospheric Model, version 3 (CAM3), *J. Clim.*, *21*(18), 4859–4878, doi:10.1175/2008JCLI2237.1.

Corresponding author: P. N. Blossey, University of Washington, Atmospheric Sciences, Box 351640, Seattle, WA 98195-1640, USA. (pblossey@uw.edu)